ORIGINAL PAPER

Synthesis and characterization of the physical, chemical and mechanical properties of isocyanate-crosslinked vanadia aerogels

H. Luo · G. Churu · E. F. Fabrizio · J. Schnobrich · A. Hobbs ·
A. Dass · S. Mulik · Y. Zhang · B. P. Grady · A. Capecelatro ·
C. Sotiriou-Leventis · H. Lu · N. Leventis

Abstract A strong lightweight material (X-VOx) was formulated by nanocasting a conformal 4 nm thin layer of an isocyanate-derived polymer on the entangled worm-like skeletal framework of typical vanadia aerogels. The mechanical properties were characterized under both quasi-static loading conditions (dynamic mechanical analysis, compression and flexural bending testing) as well as high strain rate loading conditions using a split Hopkinson pressure bar (SHPB). The effects of mass density, moisture concentration and low temperature on the mechanical properties were determined and evaluated. Digital image correlation was used to measure the surface strains through analysis of images acquired by ultra-high speed photography, indicating nearly uniform compression at all stages of deformation during compression. The energy absorption of X-VOx was plotted as a function of the density, strain rate and temperature, and compared with that of plastic foams. X-VOx remains ductile even at −180 °C, a characteristic not found in most materials. This unusual ductility is derived from interlocking and sintering-like fusion of nanoworms during compression. X-VOx emerges as an ideal material for force protection under impact.

Keywords Crosslinked vanadia aerogel · Nano-foam · Cryogenic temperature · Specific energy absorption · Split Hopkinson pressure bar · Digital image correlation

J. Schnobrich and A. Hobbs—NASA GRC Summer Intern.

H. Luo · G. Churu · Y. Zhang · H. Lu
School of Mechanical and Aerospace Engineering, Oklahoma
State University, Stillwater, OK 74078, USA
e-mail: hongbing.lu@okstate.edu

E. F. Fabrizio
Ohio Aerospace Institute, 22800 Cedar Point Road,
Cleveland, OH 44142, USA

J. Schnobrich · A. Hobbs · N. Leventis (✉)
NASA Glenn Research Center, 21000 Brookpark Road,
Cleveland, OH 44135, USA
e-mail: leventis@mst.edu

A. Dass · S. Mulik · C. Sotiriou-Leventis · N. Leventis
Department of Chemistry, Missouri University of Science
and Technology, Rolla, MO 65409, USA

C. Sotiriou-Leventis
e-mail: cslevent@mst.edu

B. P. Grady
School of Chemical, Biological, and Materials Engineering,
University of Oklahoma, Norman, OK 73019, USA

A. Capecelatro
Department of Materials Science, UCLA, 420 Westwood Plaza,
Los Angeles, CA 90024, USA

1 Introduction

Aerogels are low-density nano-porous materials with attractive properties such as low thermal conductivity and high acoustic impedance. By the same token, however, they are also extremely fragile, and that has limited their applications only to some very specialized environments, for example as thermal insulators of the electronic boxes aboard planetary vehicles such as the Mars Rovers [1]. Recently, the fragility problem was solved by casting a conformal polymer coating over the skeletal nanoparticles of typical silica aerogels prepared via a base-catalyzed sol–gel method [2]. By developing covalent bonding with their surfaces, the applied polymer coating crosslinks the nanoparticles and reinforces the structure without clogging

the pores. Thus, the bulk density typically increases by a factor of 3, while the flexural strength increases by a factor of 300 with a remaining porosity at 70% [2–4]. Crosslinked samples are able to deform by 77% compressive strain [5] without developing surface cracks, and remain stable when saturated with water.

In an effort to explore the limits of the technology, the surface of the skeletal nanoparticles was modified with amines, which became the point of departure for crosslinking with isocyanate-derived polyurethane/polyurea, epoxides and styrene [5–8]. In addition to strength, other desirable properties were also introduced into the material, as for example hydrophobicity with polystyrene crosslinked aerogels [7]. Nevertheless, experimental data show that strength-wise, it makes not much difference which polymeric system is used for crosslinking. That has been attributed to the fact that the gain in strength is related to the bond energy in the polymeric tethers connecting the skeletal nanoparticles, and for a more or less similar amount of crosslinker (i.e., amount of accumulated polymer), the total bond energy does not vary dramatically from one polymer to another [9]. Hence, the strength can probably be improved further by varying the network morphology [9, 10]. For example, incorporating 5% (w/w) carbon nanofibers into native silica aerogels can improve the mechanical properties by a factor of 3–5 without a severe penalty on the density [10]. In other words, it was reasoned that different network morphologies could dissipate loading forces more efficiently, increasing strength further. For this, one approach could be to move away from silica or other metal and semi-metal oxide aerogels with nanostructures consisting of a pearl-necklace like assembly of nanoparticles. In those structures interparticle necks are the obvious weak points where failure begins [11, 12]. In this context, it is known at least since the 1940s that sol–gel derived vanadia consists of fibers [13, 14], or more accurately of entangled worm-like nano-objects yielding a 3D structure with morphology akin to bird nests [15]. Mechanically, vanadia aerogels appear to be brittle [13–15]. However, after crosslinking, the interlocking of elongated nano-worms seems to become responsible for unique mechanical properties at both room and cryogenic temperatures, which is the focus of this paper.

Thus, following procedures described previously for silica and rare earth aerogels [2, 11, 12], we have applied an isocyanate-derived polyurethane/polyurea coating on the skeletal framework of vanadia wet gels [16]. Directed accumulation of the polymer is templated by the hydroxyl functionality of the surface of the vanadia nanoworms. The resulting composites were dried into aerogels with CO_2 taken out supercritically. Since the most remarkable feature of those materials is their mechanical strength, here we explore in detail properties as a function of the synthetic

conditions, focusing specifically on the mechanical behavior. The latter was studied using dynamic mechanical analysis (DMA) and compression testing under both quasi-static conditions and high strain rates. Testing at high strain rates was conducted using a long split Hopkinson pressure bar (SHPB) and is related to applications in force protection under impact. Mechanical properties were characterized with samples of different bulk densities as well as with moisture and water-soaked samples. The deformation and failure of samples at two different densities were observed with ultra-high speed photography. The surface deformation field was determined using the digital image correlation method (DIC) via analysis of sequential images under high strain rate loading. The stiffness, strength and ductility were also investigated at cryogenic temperatures at low, moderate and high strain rates, and the energy absorption diagram is discussed.

2 Experimental

2.1 Material preparation

Vanadium (V) tripropoxide was purchased from Sigma Aldrich (Milwaukee, WI) and used as received. Acetone was obtained from AAPER Alcohol and Chemical Co. (Shelbyville, KY). Desmodur N3200 (a hexamethylene diisocyanate oligomer) was donated courtesy of Bayer Corporation (Pittsburgh, PA). Deionized water was produced using a Millipore Milli-Q water system. Siphon grade CO_2 was obtained from BOC Gases, Murray Hill, NJ, supplied locally by Ozarc Gases.

Vanadia wet gels were prepared by copolymerization of a vanadium (V) tripropoxide solution in acetone/water by modification of Dunn's procedure [17]. In a typical process, two solutions, solution A containing 5.58 mL of deionized water (0.310 mol), 11.34 mL of acetone (0.155 mol), and solution B containing 2.4 mL of vanadium (V) tripropoxide (0.0106 mol) were cooled in an acetone/dry ice bath until ice appeared in solution A; solution B just became more viscous. Solution A was shaken vigorously until all chunks of frozen water/acetone disappeared, and at that point it was added into solution B rapidly all at once. The dark orange-red mixture (sol) was shaken vigorously for 10–15 s and it was poured directly into molds where it quickly turned to green. The molds for cylindrical samples appropriate for compression testing were polyethylene syringes (Luer-LokTM Tip, BD 10 mL, 14.35 mm ID); the molds for square cross-section samples for three point bending were square glass tubes (ACE Glass Incorporated, Vineland, NJ, part No. 8700-91, SP/4 10 mm ID); and, molds with an 8 mm × 3 mm rectangular cross section for Dynamic Mechanical Analysis (DMA) were custom-made

by ACE Glass. Square and rectangular cross-section molds were open at both ends; one end was covered with two layers of Parafilm, and the cold sol was poured from the other end, which was then also covered with two layers of Parafilm. Gelation occurred in about 1 min while the sol was still cold. Samples were left in their molds to age for 5 days. After that period, gels were removed from the molds and were placed in a large jar with fresh acetone, approximately 4–5 times the total volume of the gels. The contents of the jar were agitated periodically, and acetone was changed four times, once every 24 h. Native vanadia (VOx) aerogels were obtained by a final solvent exchange in an autoclave with liquid CO_2, which was taken supercritical and was vented off isothermally at 40 °C [3, 6].

Alternatively, acetone-exchanged wet gels were crosslinked by reaction with a Desmodur N3200 solution in acetone. For this, the fourth acetone wash was replaced by an equal volume of a solution containing 32.9 g Desmodur N3200 in 82 mL of acetone. The jar was then swirled gently after 24 h and gels were allowed to remain in the crosslinking bath for 36 h. The concentration of Desmodour N3200 in the bath was varied yielding crosslinked aerogels with different densities. Subsequently, gels were heated in an oven at 50 °C for 72 h under two different conditions: either in the crosslinking bath or in fresh acetone. Typically, crosslinked vanadia (X-VOx) aerogels cured in acetone have lower densities than X-VOx aerogels cured in the crosslinking bath. After 72 h, gels were removed from the oven and they were washed four more times with fresh acetone. Finally, they were dried with CO_2 taken out supercritically as in the case of the native samples.

2.2 Thermal, physical, chemical and moisture absorption characterization

Thermal characterization was conducted by thermogravimetric analysis (TGA) and differential scanning calorimetry (DSC). TGA was performed on a TA Instruments Model 2950 HiRes instrument at 10 °C/min under nitrogen. DSC was conducted with a TA Instruments Model 2010 apparatus also at 10 °C/min under nitrogen. The aerogel nanostructure was characterized by scanning electron microscopy (SEM) and nitrogen sorption porosimetry. For SEM, samples were coated with Au and were observed with a Hitachi S-4700 field emission microscope. For nitrogen sorption porosimetry samples were outgased at 80 °C for 24 h, and were analyzed with an ASAP 2000 Surface Area/Pore Distribution analyzer (Micromeritics Instrument Corp.). Porosity, as percent empty space, was calculated from bulk and skeletal density data; the latter were obtained using helium pycnometry on a Micromeritics AccuPyc 1330 instrument. Chemical characterization was performed by XRD, XPS, infrared and attenuated total

reflectance (ATR) infrared spectroscopy. For XRD, samples were observed in the continuous mode with a Phillips X'Pert Materials Research Diffractometer (model PW3040/60) using Cu Kα radiation ($\lambda = 1.54$ Å). The incident beam prefix module was an X-ray mirror (PW3088/18) equipped with a sealed proportional detector (PW3011/20). XPS was conducted on a KRATOS AXIS 165 XPS Spectrometer equipped with a magnesium anode at 225 W, using an electron pass energy of 20 eV. A Nicolet Nexus 470 FT-IR spectrophotometer was used to obtain both infrared spectra of powder samples in KBr pellets, as well as ATR infrared spectra across the radius of disks cut from larger monoliths.

In order to investigate the effect of moisture, samples were stored under 97% relative humidity for about 2 months in an enclosed container (desicator). The mass and volume changes were monitored during this period. The weight change was measured with a balance (Denver Instrument, APX-200, max 200 g) with resolution of 0.1 mg. The bulk density was measured by taking the mass of a cylindrical sample divided by its volume. At the end of that period, samples were tested under compression. Furthermore, since X-VOx has an open-cell nanoporous structure, it can absorb water and moisture. Water-soaked samples were prepared by immersing dry X-VOx samples into water allowing them to absorb water to reach a fully saturated state.

2.3 Dynamic mechanical analysis (DMA), compression and flexural testing at low strain rates

The complex modulus was measured using a three-point bending test on rectangular samples with nominal dimensions of $50 \times 8.5 \times 2.5$ mm^3 on a Dynamic Mechanical Analyzer Model RSA II (Rheometric Scientific Inc, Piscataway, NJ). Actual dimensions were measured by a caliper (resolution 0.01 mm) and were used to calculate the complex modulus. The flexural fixture had two roller supports with 48 mm span. Temperature steps of 4 °C between −130 and 210 °C at 1 Hz fixed flexural frequency were used in order to determine peaks in the loss tangent as a function of temperature, and identify the glass transition temperature. Specimens were allowed to shrink freely along the length and width direction on the fixture. Nominal stress and nominal strain were used in the analysis. Samples were maintained for 60 s at each temperature prior to data collection.

Crosslinked vanadia aerogels (X-VOx) have a nanofibrous structure coated conformally with a nano-layer of polymer. Since there are no standard test methods for this class of materials at low strain rates, between 10^{-4} and 10^{-1} s^{-1}, it was decided to apply the ASTM D695-02a standard (Standard Test Method for Compressive

Properties of Rigid Plastics). That standard specifies use of cylindrical specimen with a height to diameter ratio of 2. Samples used for mechanical testing were cut dry without using any lubrication liquid on a low speed diamond saw (MTI Corporation, SYJ-150A). The cut surfaces of the samples were polished using grade 600 fine silicon carbide sandpaper. Testing was conducted on an MTS-810 servo-hydraulic test machine. The recorded force was divided by the initial cross-sectional area to determine the nominal compressive stress. The recorded displacement was corrected by considering the compliance of the test system obtained by compressing the two platens directly; the corrected displacement was then divided by the initial length of the specimen to determine the nominal compressive strain. Compression tests were conducted at room temperature (23 ± 1 °C) under relative humidity $35 \pm 3\%$. The effect of polymer crosslinking was investigated through compression of native vanadia, and of X-VOx cured either in the N3200 solution or in pure acetone. The strain recovery behavior on X-VOx samples was investigated under multiple loading/unloading during the process of compression. The effect of water absorption on compression of X-VOx was determined through comparison of results obtained using both dry samples and water-soaked samples. The Young's modulus, the 0.2% offset yield stress, the ultimate compressive strength, and the ultimate compressive failure strain were determined from the stress–strain curves. For samples tested at low temperatures on MTS, an Omega CY7-SD7 silicon diode sensor suitable for cryogenic temperatures was attached to the sample surface and an Omega CYC-320 thermometer was used to measure temperature. At cryogenic temperatures, samples were tested at a strain rate of 0.365 s^{-1}. The procedure for the three-point bending tests followed the ASTM standard D790. For this, we used nonstandard rectangular samples with nominal dimensions of $8.6 \times 8.6 \times 48$ mm^3, that is a length/width ratio of 5.58. Following ASTM standard D790, the stress σ and strain ε can be determined as $\sigma = 3PL/(2bh^2)$ and $\varepsilon = 6 \, h\Delta/L^2$ [5], respectively, where P is the applied load, Δ is the displacement at the center of the beam, L is the fulcrum span, b is the width of specimen, and h is height of specimen. The flexural experiments were conducted on an INSTRON Model 4202 (Instron Corporation, Norwood, MA) universal testing machine. The crosshead speed was 10 mm/min and the fulcrum span was 40 mm. Flexural tests were conducted at room temperature (23 °C) and at −180 °C. For a beam with length/thickness ratio less than 16 as specified in ASTM D790, we considered the contribution of shear-induced deformation. Using the Castigliano's theorem [5], the flexural modulus obtained from three-point bending of a beam is determined from

$$E = \frac{PL^3}{48\Delta I}\left[1 + \frac{12(1 + v)}{5}\left(\frac{h}{L}\right)^2\right] \qquad (1)$$

where I is the moment of inertia of the cross section, and v is the Poisson's ratio.

2.4 Compressive experiments at high strain rates

Compressive experiments at high strain rates (50–2,500 s^{-1}) were conducted on a long split Hopkinson pressure bar (SHPB) under both ambient conditions at room temperature (23 ± 1 °C) and at cryogenic temperatures (−180 °C), as well as under a high relative humidity ($35 \pm 3\%$). The schematic diagram of the SHPB is shown in Fig. 1. The SHPB consists of a steel striker bar, incident and transmission bars, and a strain data acquisition system. A disk shaped X-VOx sample (13.72 mm in diameter and 2.54 mm in thickness) was sandwiched between the incident and transmission bars. The incident and transmission bars made of 304L stainless steel had lengths 7,514 and 4,049 mm, respectively, with an outer diameter equal to 19 mm. A hollow transmission bar was used to reach high signal-to-noise ratio for the transmitted signal. The inner diameter of the transmission bar was 14.1 mm. At the end of the transmission bar, an end-cap made of hard tool steel was press-fitted into the hollow tubing to support the specimen. Appropriate pulse shaping can remove the end cap effect on 1D stress wave propagation [18]. A new pulse shaper, consisting either a metal tubing placed inside another one, or two pieces of copper tubing, was used to help reach dynamic stress equilibrium state and constant strain rate, reducing the dispersion of the incident wave due to the bar geometry [19], necessary for a valid SHPB experiment. Prior work by Chen's group [18, 20] determined that the wave dispersion under 1D wave propagation is negligible when appropriate pulse shaping is used. The working principle of SHPB has been well documented in literature [20]. Under a valid SHPB experiment, formulas for the history of stress, strain rate and strain in a specimen have been also documented [18, 20, 21]. In the case of high strain rates, SHPB experiments were conducted to determine the effects of strain rate, water, moisture, absorption, and low temperature. In each SHPB experiment, five or more specimens were tested to assure repeatability under the same test conditions.

2.4.1 High-speed photography and Digital Image Correlation (DIC)

A Cordin 550–62 high speed digital camera (62 color frames, up to 4 million frames per second, 10-bit resolution CCD with 1000×1000 pixels) was used to acquire images of a specimen at a rate of 71,829 frames per second. Two

Fig. 1 Schematic diagram of the SHPB setup
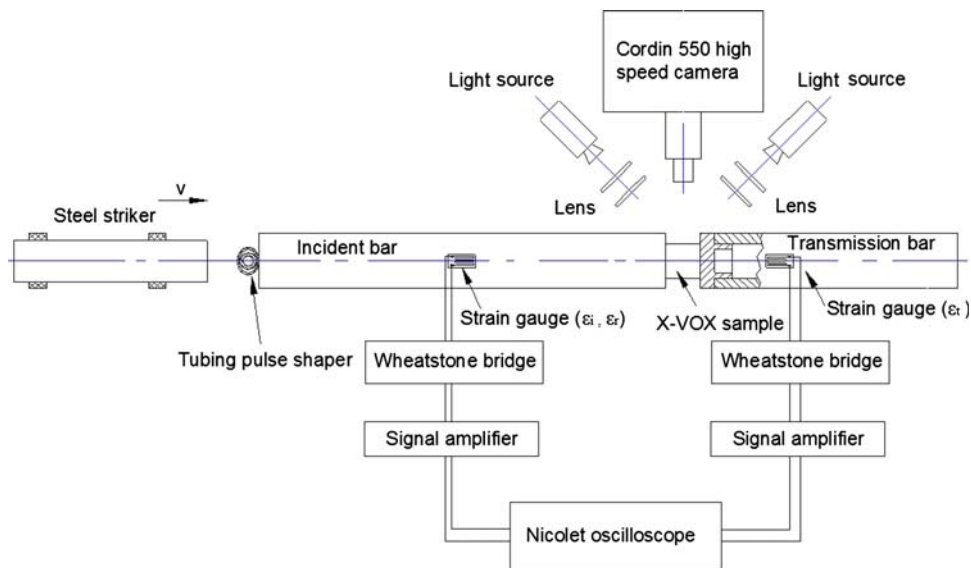
Cordin 605 high intensity Xenon light sources with two sets of lenses were used to illuminate the specimen surface. In order to reach good focus, cubic specimens with 10.4 mm side length were used for observation of deformation and failure behavior. The use of such specimens allowed the measurement of Poisson's ratio and the observation of the failure. A speckle pattern was printed on the surface facing the camera using black silicon rubber dots. The silicon rubber coating is soft with Young's modulus of about 1 MPa so that the strengthening effect is negligible. Also it was determined that the rubber does not react chemically with the X-VOx. Digital image correlation (DIC), a non-contact full-field deformation measurement method widely used to measure surface deformations [21, 22], was used to measure the latter on specimens. In DIC, two images, the reference image and the deformed image, are compared to determine the surface deformations through tracking distinct gray scale patterns. In this work, the DIC code developed by Lu and Cary [23], capable of measuring both first-order and second-order displacement gradients, was used to determine the surface deformations on a specimen.

2.4.2 Effects of density, water and moisture absorption, and low temperature

The mechanical behavior of X-VOx aerogel depends on their mass density. The effect of density on the stress–strain relationship was investigated at a strain rate of ~ 300 s^{-1}. Both water-soaked and moisture saturated X-VOx specimens were used to measure the stress–strain relationships at a compressive strain rate of ~ 330 s^{-1}. Results are compared with those from dry X-VOx specimens at room temperature. A refrigerator was used to cool samples to

-5 °C; dry ice (melting point -78 °C) was placed in a vacuum flask to cool the samples to ~ -55 °C; liquid N$_2$ (boiling point: -197 °C) in a Dewar were used for reaching cryogenic temperatures (~ -180 °C). All samples were kept at the set temperature for at least 2 h to reach thermal equilibrium. For SHPB experiments, once samples were ready for testing, they were placed quickly between the pre-cooled incident and transmission bar ends and the testing was completed within 2–3 s.

3 Results

3.1 Synthesis, physicochemical, morphological and moisture uptake characterization of vanadia aerogels

Vanadia aerogels (VOx) were prepared by supercritical fluid (SCF) CO$_2$ drying of corresponding wet gels, which in turn were prepared by a modification of Dunn's procedure [17] whereas vanadyl triisopropoxide was substituted with vanadyl tripropoxide; the latter had been used in earlier protocols [13]. Evidently, the substitution was essential for our purposes, because invariably all large monolithic gels prepared via the former vanadium source developed cracks even while still in their molds. Figure 2 schematically summarizes the preparation procedures for both native as well as polymer crosslinked samples. Cooling of the acetone/water solution and the vanadium tripropoxide sample slows gelation, which otherwise takes place upon mixing, and gives time to pour the mixture into molds. Aging for 3–5 days is important, because it strengthens the wet gels enough for gentle handling. Wet gels were solvent-exchanged by four acetone washes and they were either

dried to native vanadia aerogels (VOx) or they were subjected to a crosslinking process as described below. After SCF drying the diameter of the native VOx samples was found reduced by 22.8% relative to the diameter of the molds, the dimensions of the X-VOx samples cured in acetone with densities 0.38–0.42 g/cm^3 were reduced by 4.2–5.5%, and the dimensions of the X-VOx samples (in either cylinder or rectangular forms) cured in N3200 with density 0.58–0.66 g/cm^3 were reduced by 4.3–6.2%. These results indicate that the crosslinking process has increased the dimensional stability of vanadia aerogel monoliths. Table 1 summarizes key properties of these materials. Macroscopically, native vanadia aerogels appear green,
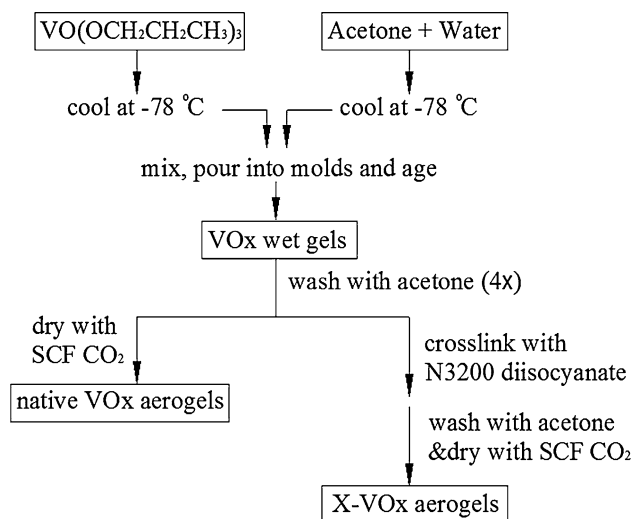

Fig. 2 Schematic preparation of native and crosslinked vanadia aerogels

suggesting the presence of vanadium (IV) [17]. They are highly porous (consisting of ~97% empty space), low-bulk density materials (~0.08 g/cm^3), which are also extremely fragile. Their BET surface areas are around 216 m^2/g, which are closer to those reported for vanadia ambigels obtained by ambient pressure drying rather than for aerogels (~300 m^2/g) prepared via SCF drying [15]. Microscopically, they consist of entangled 100–200 nm long, 30–40 nm thick worm-like objects (Fig. 3a) whose surface morphology reminds the surface morphology of secondary particles of silica aerogels [5], suggesting that they are also formed by coalescing primary particles. By closer examination of SEM images (Fig. 3a), the size of the primary particles seems to fall in the 6–8 nm range. XRD (Fig. 4a) of a native vanadia aerogel shows a nanocrystalline material with well defined, albeit broad, reflections at $2\theta = 26.37°$ and at $2\theta = 50.58°$. From the half-width of the XRD reflections we calculate (via the Scherer method) that the crystallite size is in the range of 5 nm (derived from the peak at 26.37°) and 12 nm (derived from the peak at 50.58°). On one hand this broad particle size range reflects a disorganized solid, but on the other hand it matches with the primary particle size estimated from SEM (refer to Fig. 3a). The library best-match for the observed reflections in XRD is for $V_3O_7 \cdot H_2O$, implying that vanadium (V) was reduced during processing (probably by acetone) to vanadium (IV). The presence of vanadium (IV) is quantitatively supported by the XPS data shown in Fig. 4b showing a broad vanadium $2p_{3/2}$ peak with a shoulder at lower binding energies indicating the presence of both the +5 and +4 oxidation states [24]. Thus assuming two peaks, both with 80% Gaussian and 20%

Table 1 Selected properties of vanadia aerogel monoliths as a function of preparation conditions

Sample ID/ N3200:acetone in bath (g/mL)	Bulk density ρ_b^a (g/cm^3)	Skeletal density ρ_s^b (g/cm^3)	Porosity^c (%)	BET area (m^2/g)^d (average pore diameter^e, nm)
VOx: native samples	0.078 ± 0.011	2.854 ± 0.112	97	216 (56.5)
X-VOx: samples cured in acetone				
5.5:95	0.219 ± 0.009			
11:94	0.257 ± 0.003	1.383	81	
33:82	0.421 ± 0.008	1.293 ± 0.015	67	99.7 (71.2)
X-VOx: samples cured in the N3200:acetone bath				
5.5:95	0.338 ± 0.005			
11:94	0.465 ± 0.007	1.257	63	
33:82	0.593 ± 0.004	1.236 ± 0.008	52	68.4 (109)

^{a} Average of five different samples

^{b} Single sample, average of fifty (50) measurements

^{c} Porosity = $[(1/\rho_b) - (1/\rho_s)]/(1/\rho_b)$

^{d} Single sample

^{e} Average pore diameter by the single point adsorption $4 V_{Total}$/(BET surface area) method
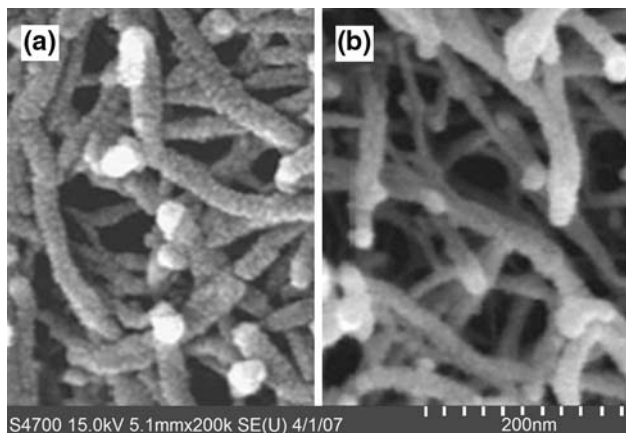
All errors represent one standard deviation

Fig. 3 Scanning electron micrographs. (**a**) a native vanadia (VOx) aerogel ($\rho_b = 0.078$ g/cm^3); (**b**) a crosslinked vanadia (X-VOx) aerogel ($\rho_b = 0.428$ g/cm^3)

Lorentzian contributions, centered at 517.8 eV (vanadium V) and at 516.47 eV (vanadium IV), with a common half-width of 1.6 eV, it is calculated that vanadium is present at 67.61% as vanadium (V) and at 32.39% as vanadium (IV), supporting the XRD assignment for $V_3O_7 \cdot H_2O$.

Infrared spectra of native vanadia aerogels (Fig. 4c-bottom, dashed line) show the strong absorption of V=O at $\sim 1,000$ cm^{-1}, while broad V–O bands appear below 900 cm^{-1}. The spectrum, however, is dominated by a broad absorption in the 3,500 cm^{-1} and a second one at 1,625 cm^{-1}, which are assigned to surface hydroxyls and adsorbed water [17]. The presence of adsorbed water is further indicated by TGA analysis (Fig. 4d) that shows a loss of $\sim 15\%$ mass at around 100 °C accompanied by a strong exothermic heat flow (by DSC) with a peak at 80 °C. The presence of adsorbed water is essential for building interparticle tethers as discussed before [3].

Thus, in analogy to our recent investigations with silica and rare earth aerogels [2–9, 12], vanadia wet gels are expected to react with isocyanates introduced in the mesopores, developing interparticle molecular tethers via formation of: (a) urethane groups by reaction with hydroxyl groups on the surface of vanadia, and (b) urea bridges with other isocyanates from the mesopores; the latter are formed by a two-step reaction sequence whereas dangling isocyanates are hydrolyzed by surface adsorbed water to yield CO_2 and dangling amines, which in turn react with free diisocyanates in the mesopores to give urea. As demonstrated in Table 1, the amount of isocyanate uptaken, and therefore the density of the resulting aerogels, can be controlled by two methods: either by varying the concentration of the diisocyanate in the crosslinking bath, or by curing the isocyanate-equilibrated wet gels in the acetone/isocyanate equilibration bath itself or in fresh acetone. The resulting crosslinked vanadia aerogels (X-VOx) were characterized by ATR-IR spectroscopy. Figure 4c-top shows two spectra, one at the edge and one at the center of a disk cut with a diamond saw off a ~ 2 cm in diameter cylindrical X-VOx monolith. These data confirm uniform

Fig. 4 Spectroscopic and thermal characterization of mesoporous vanadia. (**a**) XRD of a native vanadia aerogel VOx; (**b**) XPS of VOx; (**c**) Top: ATR infrared spectra near the center (solid line) and near the perimeter (dashed line) of X-VOx. Bottom: IR of a native vanadium aerogel (VOx, $\rho_b = 0.078$ g/cm^3, dashed line) and of neat Desmodur N3200; (**d**) TGA and DSC data of VOx ($\rho_b = 0.078$ g/cm^3) and X-VOx ($\rho_b = 0.428$ g/cm^3)
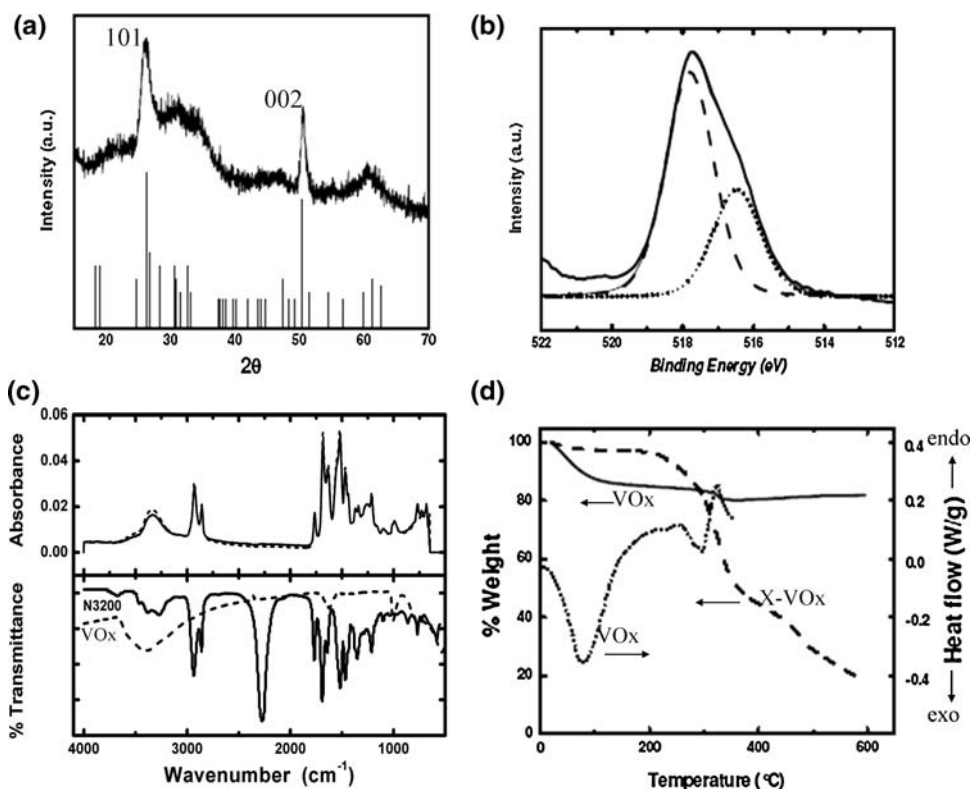
distribution of the polymer throughout the sample, and by comparison with the spectrum of neat N3200 diisocyanate (Fig. 4c-bottom solid line) the isocyanate stretch at ~2,300 cm^{-1} has disappeared completely, while the diazetidine dione stretch of N3200 at 1,767 cm^{-1} has survived the crosslinking process in analogy to X-silica and X-rare earth aerogels [3, 5, 11]. The presence of ureas in the monomer obscures observation of new ureas formed during the crosslinking process, although the relative size of the feature at ~1,695 cm^{-1} has increased. Now, Fig. 3b confirms that nanoscopically, material has been taken conformally to the skeletal worm-like objects: by comparison of Fig. 3b with 3a, the thickness of the coating for the particular crosslinked X-VOx sample is approximately 4 nm. Concurrently, the BET surface area has decreased relative to the value range of the native samples, while the average pore size has increased, reflecting restricted access to the smaller crevices on the skeletal framework by the polymer coating. The skeletal density of the crosslinked samples has also decreased relative to the skeletal density of the native samples, reflecting the weighted average density of the polymer and the underlying inorganic skeletal framework. By TGA (Fig. 4d) X-VOx samples with a bulk density of 0.421 g/cm^3 contain ~3% w/w moisture, while polymer starts decomposing above 300 °C, in analogy to corresponding X-silica or X-rare earth samples [3, 5, 12]. The mass loss up to 600 °C indicates that the same crosslinked samples consist of ~82% of isocyanate-derived polymer. This is consistent with the density gain by crosslinking of the particular VOx samples (from 0.078 g/cm^3 to 0.421 g/cm^3) corresponding to 81% w/w polymer, and also with the skeletal density change from that of native vanadia (~2.854 g/cm^3) to crosslinked vanadia (1.293 g/cm^3, for samples cured in acetone with bulk density of 0.421 g/cm^3); indeed, considering the density of Desmodur N3200 derived polyurea (1.1459 g/cm^3) [5], it is calculated that the skeletal density of a sample consisting of 82% polymer, 3% water and a balance of vanadia (15%) should be 1.398 g/cm^3.

Since the solvent concentration can affect significantly the mechanical behavior of polymers [21], the effects of water and moisture absorption on the mass density of X-VOx was also investigated. Cylindrical samples of X-VOx with 13.25 mm diameter and 36 mm length, and initial mass densities of 0.434 and 0.574 g/cm^3 were soaked in water. Also two other X-VOx cylindrical samples with initial mass densities of 0.414 and 0.592 g/cm^3, were placed inside an enclosed container with water present (producing 97 ± 1% relative humidity); those samples did not have direct contact with water and are denoted as "97% moisture". Both the mass and the volume changes of the X-VOx samples were monitored over a period of time, and the density was calculated from the measured mass and
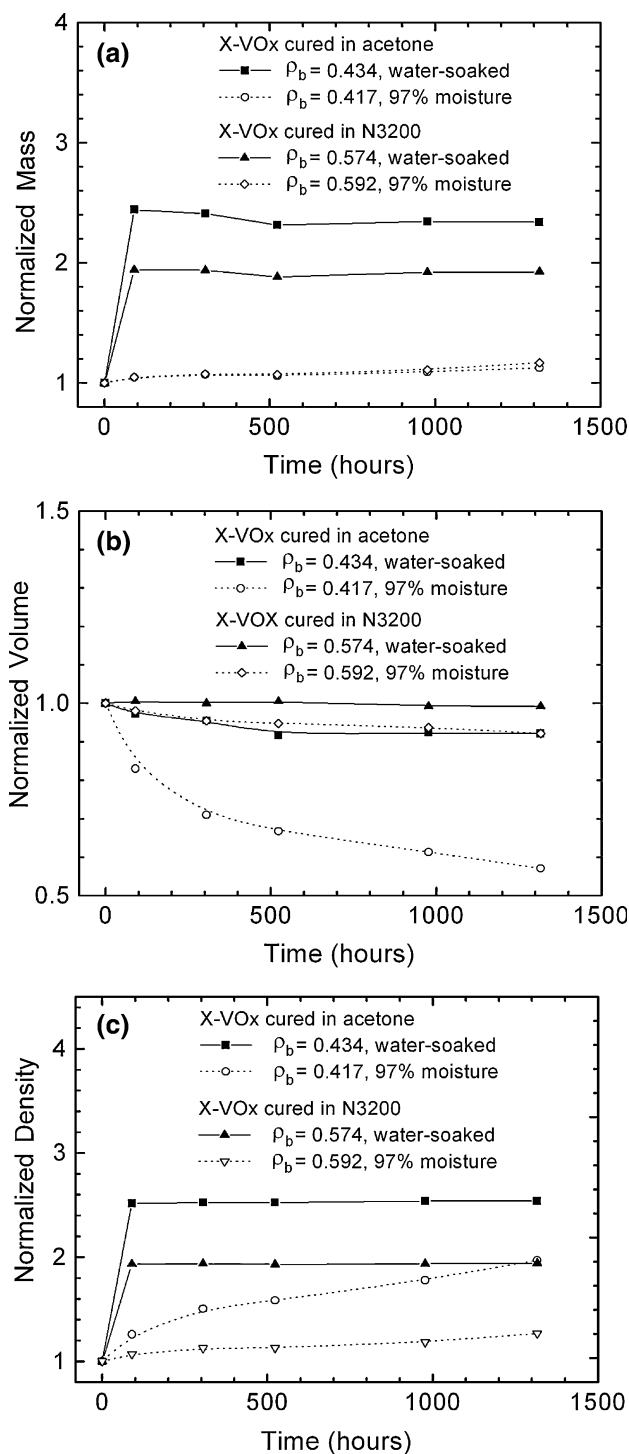

Fig. 5 Water and moisture concentration for X-VOx cured in acetone and in N3200. (**a**) percent mass gain as a function of time; (**b**) percent volume gain as a function of time; (**c**) percent mass density change history

volume. Data are summarized in Fig. 5. As shown in Fig. 5a, when samples were immersed in water, the weight gain reached a steady value in about 2 days. When samples were placed under 97 ± 1% relative humidity, the weight

Table 2 Properties for X-VOx saturated with water and exposed to 97% relative humidity (after 1,500 h)

Material	X-VOx cured in acetone			X-VOx cured in N3200		
Condition	Dry	Water	97% Moisture	Dry	Water	97% Moisture
Initial bulk density (g/cm^3)	0.414	0.434	0.414	0.588	0.574	0.592
Final bulk density (g/cm^3)	–	1.102	0.816	–	1.114	0.751
Strain rate (s^{-1})	370	360	318	321	346	345
E (MPa)	242 ± 17	271 ± 27	1227 ± 101	586 ± 16	542 ± 42	621 ± 38
$\sigma_{0.2}$ (MPa)	7.3 ± 1.5	9.9 ± 0.6	39.1 ± 3.4	16.4 ± 0.5	17.9 ± 1.8	17.9 ± 0.4

gain increased slightly and gradually, and could hardly reach a fully saturated state. Thus, in order to determine the effect of moisture concentration on the mechanical behavior, we used samples kept under 97 ± 1% relative humidity for 2 months. Table 2 summarizes the final densities of X-VOx with presence of water or solvent for four different densities of X-VOx under ambient conditions. Water did not escape from the samples after removing from the water container, indicating that water was trapped in the mesopores probably held by hydrogen bonding with dangling amines and polar groups of polyurea. The percent weight gain after immersion in water as shown in Fig. 5a, was higher for X-VOx samples with lower density (e.g. 0.434 g/cm^3) than for X-VOx with higher density (e.g. 0.574 g/cm^3). This is attributed to the fact that X-VOx samples of lower density have higher porosity allowing more water to be trapped in the mesopores. The weight gain of X-VOx samples under 97% relative humidity was much less than that of samples immersed in water and it did not depend on their initial mass density. This is in turn attributed to the fact that moisture is absorbed by the polyurea skeletal coating, which retains nearly the same percentage of moisture regardless of its thickness. Figure 5b shows the volume change as a function of time, and points out that all X-VOx samples shrink both in water and under high humidity. Shrinkage is more severe for X-VOx under moisture than in water. Larger volume shrinkages are observed for X-VOx samples of lower densities. For X-VOx with a density of 0.434 g/cm^3, the volume was reduced by 7.8% after immersion in water for 1,320 h, whereas the volume of X-VOx with density of 0.574 g/cm^3 was reduced by only 1.8% in the same period. For X-VOx with density of 0.417 g/cm^3 exposed to 97% relative humidity, the volume was reduced by 43% over 1,320 h, whereas X-VOx samples with density of 0.592 g/cm^3 shrank by only 7.9% during the same time. These results indicate that X-VOx samples with higher densities and therefore thicker polyurea coatings over their skeletal network are more capable to resist dimensional changes. Figure 5c shows the density as a function of time for X-VOx in water or under 97% relative humidity. The density of X-VOx immersed in water

increased rapidly in short times, then remained constant after 2 days; the density of X-VOx increased by 90% for X-VOx with initial density of 0.574 g/cm^3, and increased by 150% for X-VOx with initial density of 0.434 g/cm^3. The percent mass density increase is higher for samples with lower initial densities (0.417 g/cm^3) than for samples with higher initial densities (0.592 g/cm^3), reflecting the higher porosity of the former. From Table 2, the mass densities of X-VOx samples of two different densities after saturation with water were 1.102 and 1.114 g/cm^3 for samples with initial dry densities of 0.434 g/cm^3 and of 0.574 g/cm^3, respectively, whereas again the difference reflects the different porosities and therefore the volume available to be filled with water in the two samples.

3.2 Quasi-static mechanical testing

3.2.1 Dynamic mechanical analysis (DMA)

The complex modulus data (storage modulus and loss modulus) of X-VOx in acetone with density 0.654 g/cm^3 were determined between −129 and 210 °C at 1 Hz. Results are presented in terms of nominal stress and nominal strain with reference to the initial dimensions. Figure 6 shows the storage modulus, loss modulus, and loss tangent as a function of temperature. At room temperature (23 °C), the Young's modulus is 672.5 MPa and is sensitive to the density, as described in Sect. 3.3.3 below. In general, the storage modulus decreases as the temperature increases. At −119 °C, the storage modulus is 1.24 GPa; at 100 °C it is reduced to 315 MPa. Around 120 °C, the storage modulus decreases at a steep rate, thereby indicating an α-glass transition. After the rapid decrease, the storage modulus shows a slight increase. Eventually, at 207 °C the storage modulus is reduced to 24.3 MPa, i.e., about 1.95% of its value at −119 °C. Figure 6 further includes the loss modulus and the loss tangent (tanδ), which is the tangent of out-of-phase angle δ, calculated in terms of the ratio of loss modulus to storage modulus. Figure 6 shows that there is a major peak in loss tangent, tanδ, at 118.4 °C, marked with "A". That peak corresponds to a high-to-low viscosity transition, indicating that the
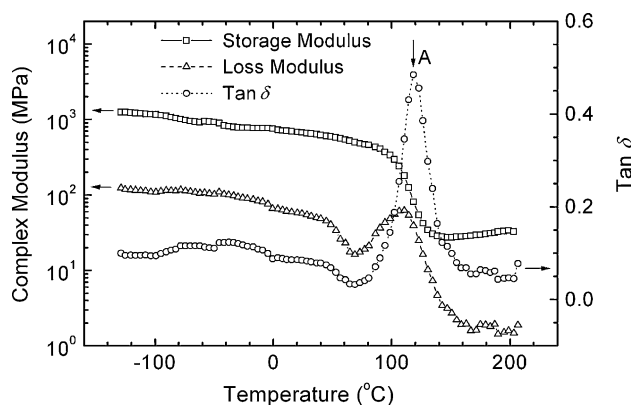
Fig. 6 Dynamic mechanical analysis (DMA) on a Desmodur N3200 cross-linked vanadium oxide aerogel (X-VOx, $\rho_b = 0.654$ g/cm^3) in a three-point bending mode with 1 Hz sinusoidal frequency
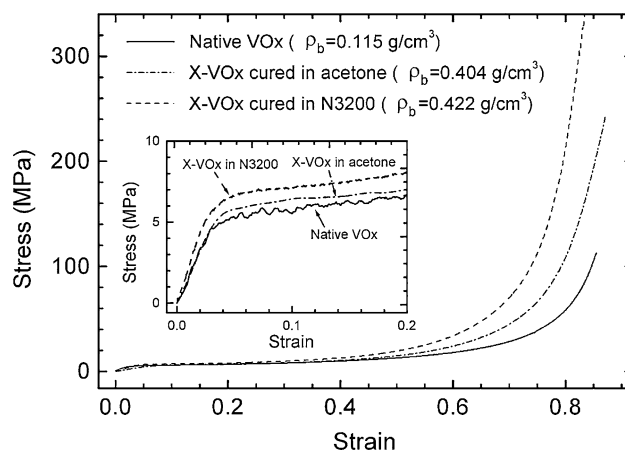

Fig. 7 Mechanical compression testing of X-VOx cured in acetone (strain rate 0.005 s^{-1}), X-VOx cured in N3200 (strain rate 0.005 s^{-1}) and native VOx (strain rate 0.0004 s^{-1}). *Inset*: Expanded curves in low strain range

material undergoes softening around that temperature. This peak is consistent with the rapid reduction in the storage modulus, thus indicating the major glass transition temperature (α-transition) at 118.4 °C. By comparison, silica aerogels crosslinked with a Desmodur N3200 isocyanate-derived polymer [5] have shown an α-transition at 130 °C, indicating a similarity of the polymer found on vanadia and to that formed on silica.

3.2.2 Quasi-static testing results

Figure 7 shows typical compressive stress-strain curves at a strain rate 4×10^{-4} s^{-1} for native vanadia and X-VOx aerogel under unconfined conditions. Native VOx aerogel are extremely brittle, developing surface cracks that lead to fragmentation as strain rate increases. The Young's modulus E, 0.2% offset yield strength $\sigma_{0.2}$, ultimate compressive strength σ_b, and ultimate failure strain ε_b as determined from Fig. 7 are listed in Table 3. This investigation focused on the characterization of the crosslinked vanadia aerogels because they are much more ductile and stronger materials than their native counterparts. Thus, after crosslinking with isocyanate, the crosslinked vanadia aerogels, or X-VOx, are about 3.5 times more dense than native vanadia samples, while all compressive stress–strain curves show three stages of deformation, a linearly elastic region under small compressive strain (<4%); a yielding regime with slight hardening until 60% compressive strain; and a densification and plastic hardening range until 84% ultimate compressive strain. The inset of Fig. 7 shows the zoomed-in initial stress–strain curves, indicating that both (native) VOx and (crosslinked) X-VOx samples have similar Young's modulus and yield strength at low strain rate. From Fig. 7 inset, at a strain rate of 5×10^{-3} s^{-1}, X-VOx cured in acetone ($\rho_b = 0.404$ g/cm^3) has lower Young's modulus, yield strength and ultimate compressive

strength than those of X-VOx cured in N3200 ($\rho_b = 0.422$ g/cm^3). Crosslinked vanadia aerogels cured in either N3200 or acetone have much higher ultimate compressive strength than that of native VOx's. The specific energy absorption is 87.5 J/g for X-VOx of density 0.422 g/cm^3 under quasi-static loading. A sample with density 0.404 g/cm^3 expands laterally in the initial compression, but does not expand further until about 60% compressive strain, as the material is mostly absorbed within its own porosity. Figure 8 shows typical X-VOx samples before and after compression testing. At failure, despite the splitting of the sample and the development of numerous cracks emanating in the radial direction, the outer layer of all crosslinked samples did not shatter into fragments, but instead the sample remained in a single piece. The significant increase in ductility over the native vanadia aerogel can be tracked to the fact that the polymer coating reinforces the weak connection between the fibrous nanostructures.

Figure 9 shows the stress–strain curve with seven loading/unloading/reloading cycles. All unloadings exhibit nonlinear recovery. Prior to each unloading, there was a loading event with increase in stress and strain. At the beginning of each unloading, even though the stress starts decreasing, the strain would keep increasing due to a memory effect, resulting in a negative slope (stiffness) in the initial unloading stage of each cycle. That memory effect is due to the polymer coating, which exhibits viscoelastic behavior. Reloading does not follow the unloading curves, resulting in hysteresis loops seen in each unloading/reloading cycle. The unloading curve becomes steeper at higher compressive strain levels (e.g., between 68 and 76%), indicating a reduced elastic behavior for samples having experienced higher level of densification by compaction. Figure 9 also shows a single stress–strain

Table 3 Selected compressive strength data of X-VOx under quasi-static compression

Materials	ρ_b (g/cm³)	Strain rate (s⁻¹)	E (MPa)	$\sigma_{0.2}$ (MPa)	σ_b (MPa)	ε_b	Condition	Length/Diameter
Native VOx	0.115	0.0004	215.8	3.73	114.3	0.86	Dry, 23 °C	2:1
X-VOx in acetone	0.404	0.005	217.5	5.02	222.2	0.84	Dry, 23 °C	2:1
X-VOx in N3200	0.466	0.0004	287.0	5.29	347.0	0.83	Dry, 23 °C	2:1
X-VOx in N3200	0.422	0.005	229.5	5.22	393.0	0.84	Dry, 23 °C	2:1
X-VOx in acetone	0.996	0.005	124.0	2.94	78.4	0.83	Water, 23 °C	2:1
X-VOx in N3200	0.650	0.365	623.3	17.3	236.1	0.79	Dry, 23 °C	2:1
X-VOx in N3200	0.650	0.365	1083.4	33.5	102.3	0.28	Dry, −180 °C	2:1
X-VOx in acetone [16]	0.436	0.005	206.0	5.60	2,183[a]	0.91	Dry, 23 °C	1:1
X-VOx in acetone [16]	0.444	0.05	438.0	13.6	890	0.82	Dry, −196 °C	1:1

Notes: mechanical data reported here represent one 5–8% standard relative deviation, not shown in this table. [a] The compressive stress of 2.18 GPa corresponds to a compressive strain of 91%

Fig. 8 X-VOx samples before ($\rho_b = 0.420$ g/cm³) and after ($\rho_b = 1.024$ g/cm³) quasi-static compression testing
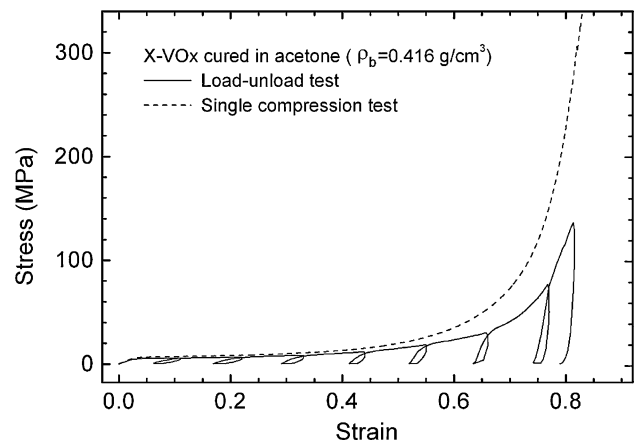

Fig. 9 Load-unload testing of X-VOx cured in acetone with bulk density $\rho_b = 0.416$ g/cm³

curve of X-VOx without unloading at the same strain rate. By comparison, the curve with multiple loading/unloading is lower than the single monotonic loading curve. Again, this is most likely due to viscoelastic effects induced by the polymer nanocoating, which results in a memory effect so that as long as unloading is applied the subsequent curve will be affected and will be adjusted lower than a monotonic loading curve.

The effect of strain rate on the mechanical behavior was first evaluated under quasi-static loading conditions. Figure 10 shows the stress–strain curves at strain rates 4×10^{-4}, 5×10^{-3}, and 4×10^{-2} s⁻¹ for X-VOx cured in N3200 (0.422 g/cm³ ≤ ρ_b ≤ 0.466 g/cm³). The Young's modulus, 0.2% offset yield strength, ultimate compressive strength and ultimate compressive strain as determined from Fig. 10 are also summarized in Table 3. Figure 10 inset shows the zoomed-in initial curves at the low strain range. Except the slight mass density effects, as the strain rate changes by two orders of magnitude, the overall stress–strain curves do not exhibit significant changes, indicating that at these low strain rates, the mechanical

behavior for X-VOx does not have a strong dependence on the strain rate. For ballistic applications where energy absorption at high speed impact is important, further testing at high strain rates using a split Hopkinson pressure bar would be necessary and the results are presented in next section.

The effect of water absorption was investigated by comparing compression testing results using both dry and water-soaked samples. After immersing a X-VOx sample in water for two days (the minimum time for water to saturate, for more details see Sect. 3.1), the sample reached fully saturated state, and gained weight by 140% with an increase in volume of less than 0.5%, indicating that water enters mostly the pores without causing the worm-like nanofibers to expand or the structure to collapse. Figure 11 compares the stress–strain curves for both dry and water-soaked X-VOx samples at a strain rate of 5×10^{-3} s⁻¹. The inset in Fig. 11 shows the obvious difference at the initial stress–strain curve at low strain range. The Young's modulus, 0.2% offset yield strength, ultimate compressive strength and strain in Fig. 11 are also summarized in
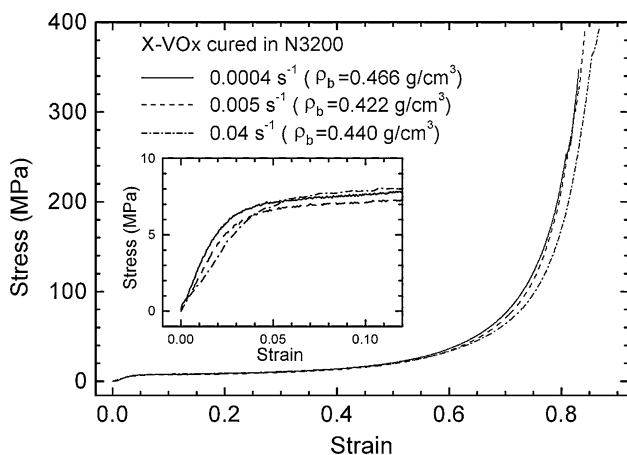
Fig. 10 Effect of low strain rate on the behavior under compression of X-VOx cured in N3200. *Inset*: Expanded curves in low strain range
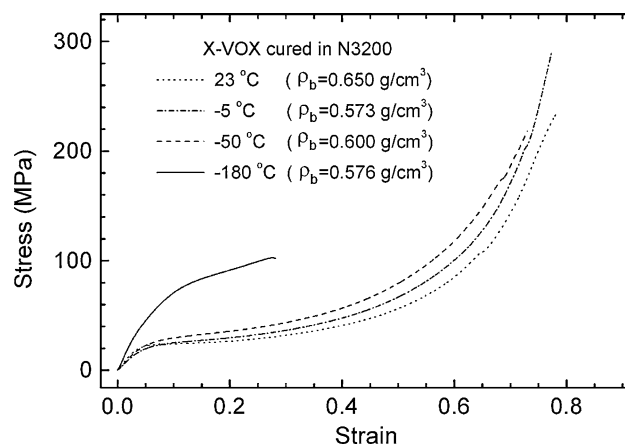

Fig. 11 The static compressive curve for both dry and water X-VOx cured in acetone (strain rate 0.005 s^{-1}). *Inset*: Expanded curves in low strain range

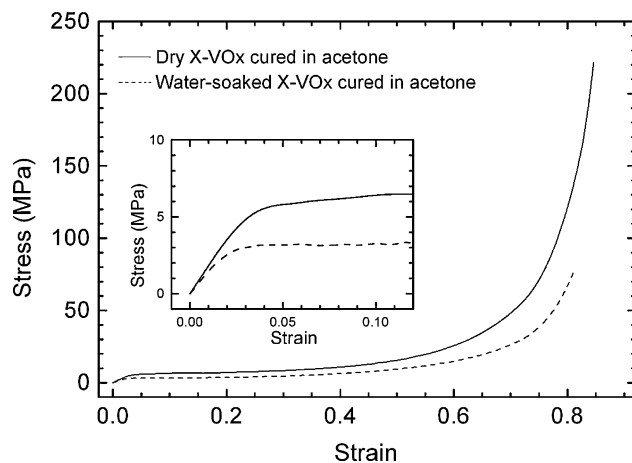Fig. 12 Compression results for X-VOx cured in N3200 at different temperatures (strain rate 0.365 s^{-1})

remains ductile until 30% compressive strain and ultimately breaks in buckling failure. The X-VOx samples have higher densities (0.57–0.6 g/cm^3) and under compression at cryogenic temperature (−180 °C) they are weaker than X-VOx samples of lower density (0.44 g/cm^3) [16]. The mechanical properties at cryogenic temperature are summarized and compared in Table 3. This indicates that the length/diameter ratio should be reduced in SHPB testing to prevent from buckling in testing at high strain rates.

Figure 13 shows the stress–strain curves obtained through three-point bending tests of X-VOx with 0.50 g/cm^3 at 21 and −180 °C. The flexural strength obtained through three-point bending provides an estimate of the tensile strength for a material in the case where tensile tests cannot be conducted readily. The flexural modulus of X-VOx with mass density of 0.50 g/cm^3 is calculated as 918/529 MPa at cryogenic/room temperatures, respectively, which corresponds to a 78% increase in the flexural modulus at the cryogenic temperature as compared with room temperature. That increase is slightly higher than the increase observed with crosslinked silica aerogels at a density of 0.48 g/cm^3, which show an increase in the flexural modulus of 70%, from 439 MPa at room temperature to 748 MPa at the cryogenic temperature [5]. At a higher density, the flexural modulus is higher than that under compression, showing the correct trend. It is noted, however, that the flexural modulus determined for X-VOx tends to be higher than the Young's modulus determined from compression tests even after the effect of density has been considered, possibly due to the difference in stress states between these two types of testing. The results appear to suggest that the flexural modulus follows a scaling law with an exponent that is different from that under compression. Further testing is needed to determine the scaling law for flexural modulus as a function of the bulk density. The stress-strain curves of Fig. 13 are linear
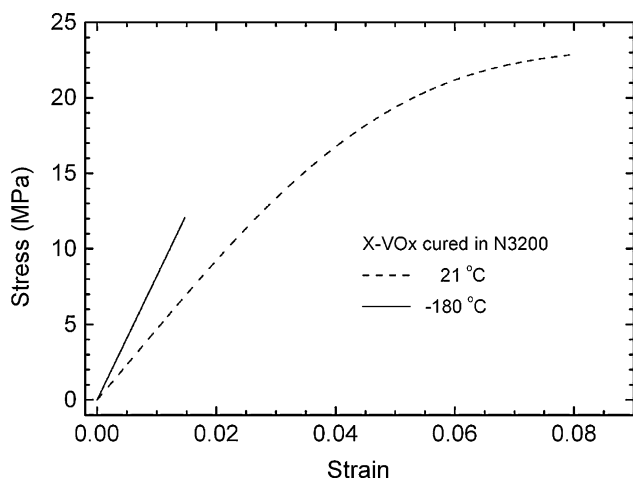
Table 3. The stress–strain curves as shown in Fig. 11 indicate that the water-soaked sample is weaker than a dry sample. The Young's modulus, yield strength, and ultimate compressive strength of water-soaked X-VOx decreased by 20%, 43% and 64%, respectively, compared to dry X-VOx. But remarkably, the water-soaked samples were still stable, did not dissolve in water, and were still ductile, albeit not as much as the dry samples. The water-soaked sample failed at an ultimate compressive strength of 78.4 MPa at an ultimate compressive strain of 83%, similar to the dry samples.

Figure 12 shows compression results of X-VOx at low temperatures at a strain rate of 0.365 s^{-1}. As the temperature decreases, the material becomes stiffer, and the stress–strain curve is shifted upwards. This indicates that X-VOx can still absorb significant amounts of energy at lower temperatures (−5 and −50 °C). Furthermore, as the temperature decreases to about −180 °C, the sample still

Fig. 13 Three-point bending tests on X-VOx aerogel rectangular samples with nominal dimensions of $8.6 \times 8.6 \times 48$ mm ($\rho_b = \sim 0.50$ g/cm^3)

Fig. 14 SEM images of the morphological changes X-VOx cured in N3200 after compression ($\rho_b = 0.64$ g/cm^3, strain rate 0.365 s^{-1}). (**a**) at initial stage (0% strain); (**b**) at 25% strain; (**c**) at 50% strain; (**d**) at 75% strain

only during the initial 2% strain range at room temperature, and then they become nonlinear from 2–8% strain until final failure with flexural strength of 22.9 MPa. The flexural strength at cryogenic temperatures is 12.07 MPa at 1.5% strain, that is 14% higher than what has been observed with crosslinked silica aerogels [5], thereby confirming the capability of X-VOx to sustain more bending loads than the latter at cryogenic temperatures.

The morphological changes of X-VOx under static compression were evaluated by SEM (Fig. 14) and porosity/surface area analysis (Table 4). X-VOx samples with density 0.64 g/cm^3 were loaded at a strain rate of 0.365 s^{-1} up to 0%, 25%, 50% and 75% strain, respectively and subsequently unloaded and the compressed samples were analyzed. For intact samples without any deformation, the porous microstructure of X-VOx with high density 0.64 g/cm^3 shows thicker polymer coating on the vanadia nanoworms than on the X-VOx samples with lower density (e.g., 0.428 g/cm^3, see Fig. 3b). Surface area analysis, shows that the surface area and the average pore diameter decreases, as the plastic deformation increases, consistent with a nanoporosity loss as particles are crushed closer with nearly no internal voids remaining between the skeletal worm-like objects under 50% strain (Fig. 14c). Also the particle diameter increases gradually from 86.5 nm (Fig. 14a), to 135.8 nm (Fig. 14b) to 253.9 nm (Fig. 14c). This behavior is different from that demonstrated by crosslinked silica aerogels [5], where particles come closer during compression but their size remains unchanged. Ultimately, at near failure (75% strain), the particle diameter dramatically increase to 5877.4 nm (Fig. 14d). The worm-like object appear fused together as if the coated polymer melted and solidified again, an interesting
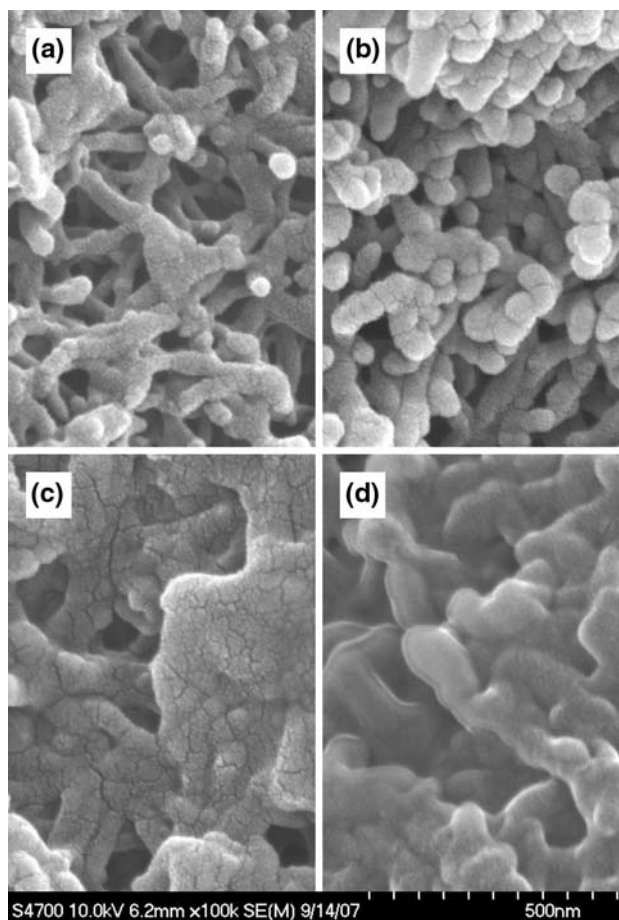
phenomenon not observed in crosslinked silica aerogels [5]. Table 4 lists an increase of the particle diameter from 86 nm to 5877 nm when a compressive strain of 75% was applied; however, Fig. 14d mainly shows a fusion of the vanadia nanoworms. The particle diameter is measured by porosity/surface area analysis and it is an average result over a much larger sample size.

Overall, for quasi-static compression, X-VOx with density of 0.422 g/cm^3 has an average yield strength of 5.22 MPa, an ultimate compressive strength within 240–370 MPa (at low strain rates in the 0.0004 to 0.05 s^{-1} range) and an ultimate compressive failure strain as high as 84%. Under three-point bending at cryogenic temperatures, the flexural modulus and strength of X-VOx with density 0.5 g/cm^3 were determined as 918/12.07 MPa, respectively, which are higher values than what has been reported with crosslinked silica aerogels. For comparison with other materials, specific properties, such as the specific Young's modulus and specific yield strength, are calculated using the absolute properties divided by the bulk density [25].
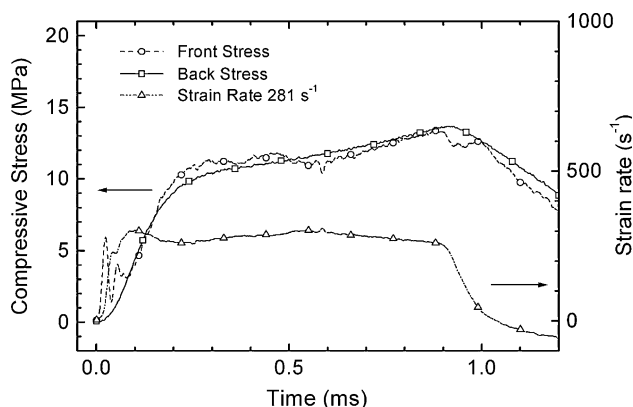
Table 4 Surface area analysis of X-VOx after compression ($\rho_b = 0.64$ g/cm^3)

Strain (%)	Porosity (%)	BET surface area (m^2/g)	Average pore diameter (nm)	Particle diameter (nm)
0	71	49.4	87.4	86.5
25	54	35.1	59.2	135.8
50	29	20.0	39.7	253.9
75	29	0.85	10.3	5877.4

The specific energy absorption determined from the area enclosed by the stress–strain curve divided by the mass density, is 87.5 J/g, indicating that X-VOx is especially suitable for force protection such as for energy absorption in automobile collision and armor applications.

### 3.3 Compression at high strain rates using SHPB

We next present results on X-VOx obtained using a long split Hopkinson pressure bar. In a SHPB test, a dynamic equilibrium state, indicated by equal stresses applied on both ends of the specimen, must first be established. Such an experiment is then considered valid and the acquired experimental data are processed to deduce the dynamic stress–strain relations. To examine the dynamic equilibrium condition, following either the 1-wave (transmitted wave), or the 2-wave (difference between incident wave and reflected wave) method [19, 20, 26], the front stress (at the end of the specimen in contact with the incident bar) and the back stress (at the end of the specimen in contact with the transmission bar) are compared as a function of time. The results, together with the strain rate history are given in Fig. 15. The front stress is very close to the back stress, indicating that the dynamic equilibrium condition was nearly established and the specimen was nearly uniformly deformed except during the initial 100 µs rising-up stage. With the use of pulse shaping, the strain rate is nearly constant during most of the loading stage with only

a slight variation ($\sim 2.5\%$), indicating that the specimen deformed somewhat under a constant strain rate. Then the incident, transmitted and reflected signals were processed further to determine the stress–strain relation at high strain rates.

3.3.1 Effect of strain rate

Compressive stress–strain curves for X-VOx under unconfined conditions at several strain rates within the 50–2,500 s^{-1} range are shown in Fig. 16. In general at those high strain rates X-VOx samples are linearly elastic under small strains (<3%). Then they yield at $\sim 3\%$ compressive strain and exhibit uniform compaction until $\sim 50\%$ strain. Subsequently, X-VOx samples are densified and fail at ultimate compressive strains of 60–70%. Since the length of the bar allows loading duration time of 1.5 ms, at a medium strain rate, the maximum attainable strain within 1.5 ms was lower than that at a higher strain rate. Consequently, at medium strain rates, the specimen did not break during experiments so that the compressive stress–strain curves shown in Fig. 16 are not the complete curves. This situation was encountered at strain rates of 50, 70, 281, and 334 s^{-1} (Fig. 16). At strain rates above 1,000 s^{-1}, all samples failed so that the compressive stress-strain curves shown are complete. X-VOx samples become stiffer as strain rate increases. Thus, the mechanical behavior of

Fig. 15 Typically dynamic stress equilibrium status and constant strain rate of X-VOx
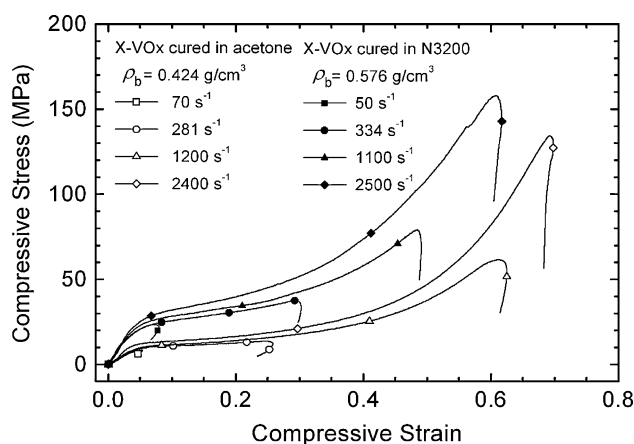
Fig. 16 Dynamic stress–strain curves of X-VOx cured in acetone ($\rho_b = 0.424$ g/cm^3) and N3200 ($\rho_b = 0.576$ g/cm^3)

X-VOx depends highly on the strain rate at high strain rates.

Figure 17 shows the SEM images before and after SHPB testing for X-VOx with density 0.424 g/cm^3. The original X-VOx nano-structure exhibits the usual nano-porous framework (Fig. 17a). After compression on the SHPB impact at 60% plastic strain under a strain rate of 1,200 s^{-1}, most of nanopores disappeared and vanadia nano-worms with their polymer coating were fused together to form aggregates of larger nano-worms (Fig. 17b), which are ~600 nm long and ~100–150 nm thick. It is perhaps the fusing of nano-worms that allows X-VOx to be much more ductile than crosslinked silica aerogels and not to break into fragments even when radial splitting occurs. After compression at 60% strain the BET surface area was reduced from 54 m^2/g to 17 m^2/g indicating a massive structural change. Indeed, the bulk density has increased from 0.436 g/cm^3 to 0.75 g/cm^3 while the skeletal density has remained about unchanged (1.298 g/cm^3 before to 1.293 g/cm^3 after compression). The porosity has been reduced from 68% before compression to 42% after. Clearly, compression causes collapse of the mesostructure while the worm-like skeletal objects are nearly incompressible, therefore already compact with no internal voids. SEM after compression (Fig. 17b) confirms that porosity has practically disappeared while skeletal nanoworms seem fused together even though the bird-nest nanomorphology is still clearly visible. Future investigation is needed to determine the temperature profile during compression at high strain rates and thus the mechanism for nano-worm fusion.

Both the Young's modulus data and the 0.2% offset compressive yield strengths are plotted in Fig. 18, as a function of the strain rate. The yield strength increases with
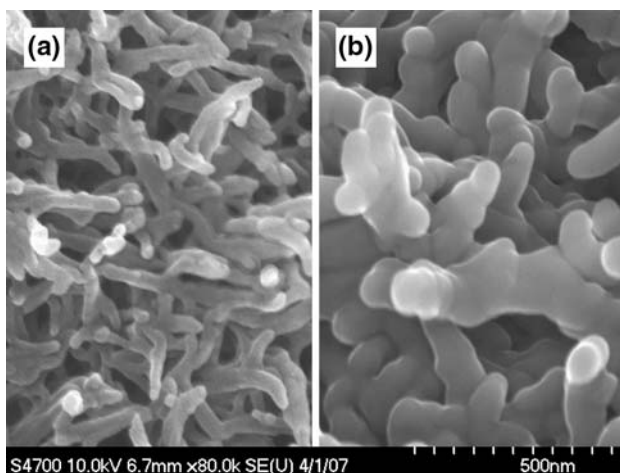

Fig. 17 Scanning electron micrographs of X-VOx. (**a**) before impact ($\rho_b = 0.436$ g/cm^3); (**b**) after SHPB impact ($\rho_b = 0.75$ g/cm^3, strain rate 1,200 s^{-1}, limit strain 62%)
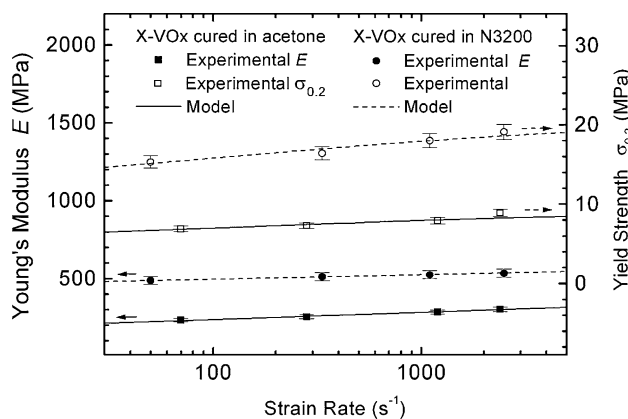

Fig. 18 Young's modulus E and yield strength $\sigma_{0.2}$ as a function of strain rates for X-VOx samples

the strain rate. The relationship between yield strength and strain rate is fitted to the model given [27],

$$\frac{\sigma_{0.2}}{\sigma_0} = 1 + \frac{2}{\pi} C_1 \tanh \left[\ln \left(\frac{\dot{\varepsilon}}{\dot{\varepsilon}_0} \right)^{m_1} \right] \qquad (2)$$

where $\sigma_{0.2}$ is the 0.2% offset compressive yield strength; σ_0 is a reference compressive strength; $\dot{\varepsilon}_0$ is the reference strain rate; C_1 and m_1 are constants. As seen in Fig. 18, this model can describe the yield data reasonably well. The Young's modulus increases also with the strain rate. The threshold strain to reach dynamic stress equilibrium is ~2%, corresponding to 100 μs rising-up time. The Young's modulus data are considered to be valid because the dynamic equilibrium state was established below the limit of linearity. Following the relationship established for other materials such as crosslinked silica aerogels [21] and plastic foams [25], the Young's modulus is given as a function of strain rate by,

$$\frac{E}{E_0} = C_2 \left(1 + \ln \left(\frac{\dot{\varepsilon}}{\dot{\varepsilon}_0} \right)^{m_2} \right) \qquad (3)$$

where E_0 is a constant, taken as 1 GPa; C_2 and m_2 are constants. From the experimental data, the best-fit constants C_1, C_2, m_1 and m_2 are summarized in Table 5. This model can also describe the experimental data very well, as seen in Fig. 18. The specific energy absorption values are 63.3 and 81.8 J/g for X-VOx at densities 0.424 g/cm^3 and 0.576 g/cm^3, cured in acetone and in N3200, respectively, at a strain rate of ~2.400 s^{-1}, determined from the curves shown in Fig. 16.

3.3.2 High speed photography and Digital Image Correlation (DIC)

A Cordin 550-62 high-speed digital camera was used to acquire images of the sample surface during SHPB tests, in order to observe the failure behavior at high strain rates.

Table 5 Model parameters used for Young's modulus and yield strength

Materials	ρ_b (g/cm³)	n_1	n_2	m_1	m_2
X-VOx cured in acetone	0.39–0.66	1.87[a]	2.30[a]	0.45	0.083
X-VOx cured in N3200		1.83[b]	2.03[b]	0.45	0.024
X-silica [21]	0.45–0.73	3.10	3.10	0.10	0.40
Silica aerogel [34]	0.08–0.4	3.7 ± 0.2	2.6 ± 0.2	–	–
Silica aerogel [28–30]	0.005–2.7	2.59 ~ 3.53	–	–	–
C aerogel [30]	0.06–3.5	2.69 ± 0.05	–	–	–
RF aerogel [30]	0.15–1.5	2.95 ± 0.10	–	–	–
MF aerogel [30]	0.04–1.1	3.13 ± 0.07	–	–	–
Silica aerogel [30, 32, 33]	0.1–2.5	3.6	2.6	–	–

Notes: "–" Indicates that data was not available; [a] The exponent at low strain rates from testing on MTS; [b] The exponent at high strain rates from testing on SHPB

Surface deformations were determined using the digital image correlation technique. Among the total of 62 color frames, four typical frames are shown in Fig. 19. Speckles were firmly imprinted on the specimen surface using black silicone rubber dots. A ruler with a grid of 1 × 1 mm was fixed on the base of the SHPB, also in order to be recorded by the camera as spatial reference. Thus, Fig. 19a shows the image of the specimen prior to loading at time 0 µs. After 724.0 µs, as shown in Fig. 19d, the specimen has been compressed by about 55% strain, but it did not show any formation of surface cracks, indicating an extremely ductile behavior under high speed impact. It is reminded that under quasi-static compression on an MTS system, at ~70% compressive strain, a X-VOx sample developed surface cracks as shown in Fig. 8. In compression at high strain rates, the applied compressive strain was limited by the loading duration of the SHPB which is 1.5 ms in this setup, so that it did not reach a value high enough to cause formation of surface cracks. However, this limit strain is enough for the following DIC analysis of the strain field.

The Digital Image Correlation (DIC) technique was used to determine the surface strain distribution on a specimen. Each pixel represents a length of 37.04 µm in both horizontal and vertical directions. Development of surface deformations was determined using Fig. 19a as the reference image. The strains, determined from the bar waves and from DIC (marked by "DIC"), are synchronized with the stress determined from the transmitted wave, and
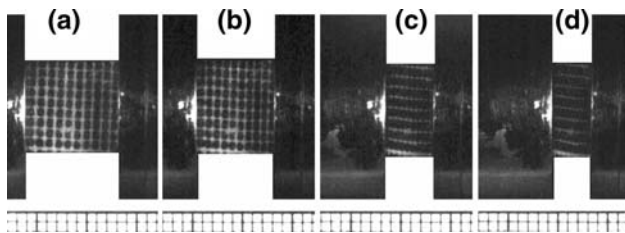
are plotted in Fig. 20. Under very high compressive strains, as in the case of Fig. 19d, speckles are too close to be discerned so that deformations can no longer be determined from DIC. Consequently, deformed images after Fig. 19d do not render any useful data points for the DIC method. From Fig. 20, the data points from DIC agree well with data obtained from analysis of the waves recorded by the strain gauges attached to the bars, providing further assurance on the validity of the compression data at high strain rates. In Fig. 20, the transverse strain (strain in the vertical direction) determined from DIC is also plotted with the axial strain. The Poisson's ratio was determined from these results, and its average value is 0.152 ± 0.008. In comparison, vitreous glass has a Poisson's ratio close to 0.2 in the elastic regime (<5%). For X-VOx, however, the Poisson's ratio maintains the low value of 0.152 even at 34% compressive strain. Under such a high compressive strain, most solids have a much higher Poisson's ratio, close to 0.5. The low Poisson's ratio in the X-VOx indicates that the material is in general absorbed by its own porosity so that lateral deformation is minimal.

Figure 21a and b show the contours of displacements in the horizontal and transverse directions, respectively, as determined from DIC on image "d" of Fig. 19. Figure 21c and d show the contour of strain field in the horizontal and
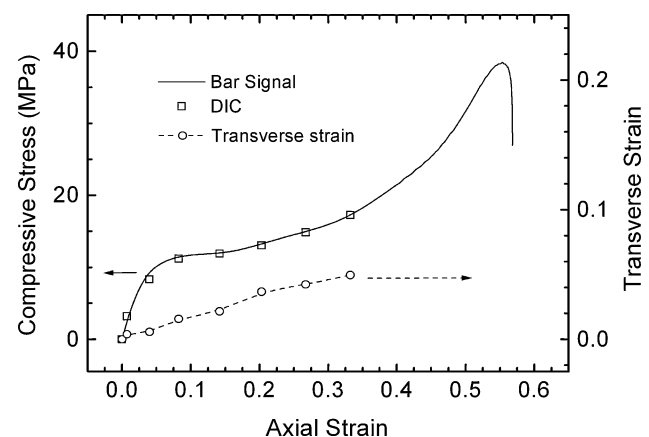

Fig. 19 High-speed deformation images of X-VOx cured in acetone ($\rho_b = 0.416$ g/cm³) on SPHB testing. The lines of rulers on the bottom are spaced 1 mm apart. (**a**) at 0 µs; (**b**) at 306.3 µs; (**c**) at 570.8 µs; (**d**) at 724.0 µs

Fig. 20 Compressive stress–strain curves of X-VOx cured in acetone ($\rho_b = 0.416$ g/cm³) determined from bar signals and DIC

transverse direction, respectively. These results show that surface deformations on samples are relatively uniform in the central region, indicating that compaction occurs relatively uniformly throughout the specimen. The average axial compressive strain for the strain field as shown in Fig. 21c is 26.74 ± 0.05%, very close to the strain 26.14% as calculated from strains recorded by the gauges attached to the bars.

3.3.3 Effect of mass density

X-VOx samples with different densities were compressed on the SHPB to determine the effect of density on the stress–strain relations. As described in Sect. 3.1, X-VOx samples with higher densities were prepared by applying a thicker conformal polymer coating on the skeletal framework, by curing the samples in a N3200 solution rather than in pure acetone and through change of the concentration of N3200. Figure 22 shows the stress–strain relations for native VOx and X-VOx samples at four different densities at strain rates close to 300 s^{-1}. It is noted that in dynamic testing, it is difficult to reach exactly the same strain rate in different experiments. The testing at a strain rate near 300 s^{-1} is considered to reveal primarily the effects of density on the stress–strain relationship. The curves are not complete due to the limitation imposed by

the 1.5 ms loading duration; therefore, they do not show the total behavior throughout the failure of the sample. Results indicate that the stress–strain relationship is very sensitive to the mass density at these strain rates. At all densities, the stress–strain curves show similar trends, namely, an elastic, range, followed by compaction and by plastic hardening and densification. At higher mass densities, X-VOx exhibits higher stiffness and higher strength, giving curves above those at lower densities. Figure 23 shows the variation of both the Young's modulus and the 0.2% offset compressive yield strength as a function of mass density. Young's modulus and yield strength (or plastic collapse stress) were fitted into the following power law [21, 28–34] relations

$$\frac{E_b}{E_s} = C_3 \left(\frac{\rho_b}{\rho_s} \right)^{n_1} \tag{4}$$

$$\frac{\sigma_b}{\sigma_s} = C_4 \left(\frac{\rho_b}{\rho_s} \right)^{n_2} \tag{5}$$

where E_b and E_s, σ_b and σ_s, ρ_b and ρ_s are Young's modulus, yield strength, and mass density of the corresponding bulk and skeletal materials, respectively; C_3 and C_4 are constants and depend on the material skeletal density, while n_1 and n_2 are density exponents that do not depend

Fig. 21 Contours of displacements and strains of X-VOx cured in acetone ($\rho_b = 0.416$ g/cm^3) determined from DIC. (a) axial displacement field U (unit: 1 pixel = 37.04 μm); (b) transverse displacement field V (unit: 1 pixel = 37.04 μm); (c) axial strain field; (d) transverse strain field
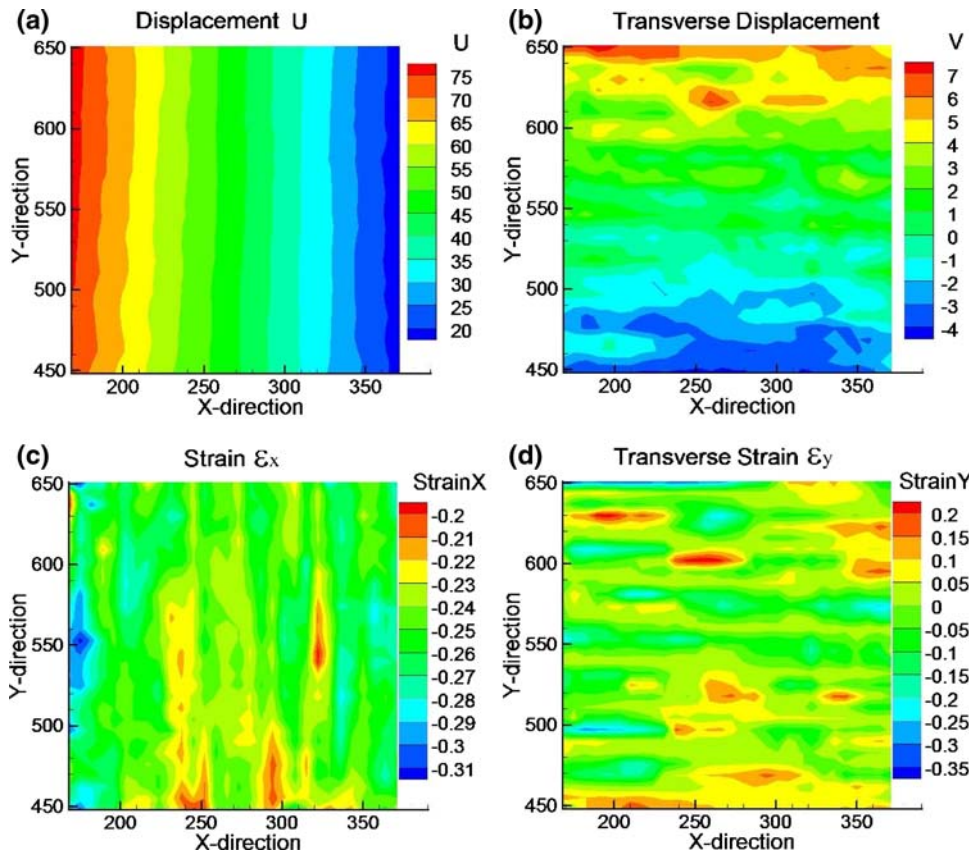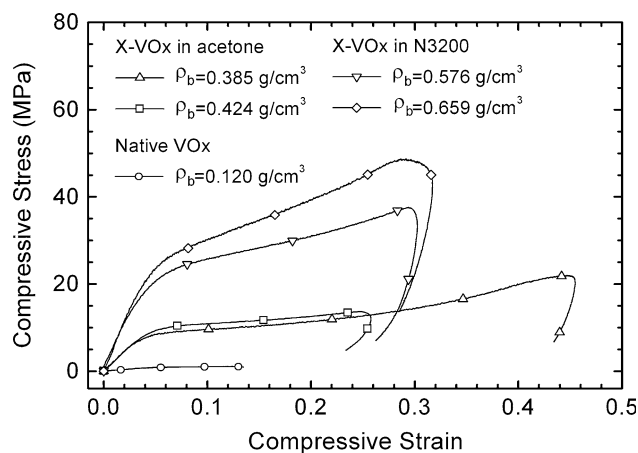
Fig. 22 Stress–strain curves of X-VOx at several densities (strain rate $\sim 300 \, s^{-1}$)

on the material skeletal density. The modulus and the strength data are fitted into Eqs. 4 and 5 for a given strain rate ($\sim 300 \, s^{-1}$), and the best-fit parameters are listed in Table 5 using $E_s = 1$ GPa, $\sigma_s = 10$ MPa, and $\rho_s = 1.0$ g/cm^3. The fitted curves plotted together with the experimental data as shown in Fig. 23. The difference between the experimental data and model is within 5%. The best-fit parameters are summarized in Table 5. The parameters at low strain rates are close to that at high strain rates. For comparison, the exponents for several other aerogels, namely silica aerogel, carbon aerogel and organic aerogel, are also listed in Table 5. The results show that the mechanical properties of X-VOx are less sensitive to the mass (bulk) density than other types of aerogels, such as native and crosslinked silica aerogels [5], carbon aerogels etc. [28–34]. That different behavior is most likely due to the difference in morphology. X-VOx shows a nanoworm nanostructure while in other types of aerogels, the pearl-necklace type of structure dominates. Further investigation
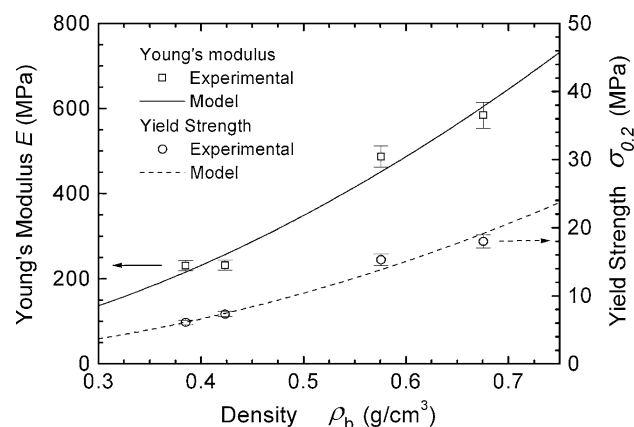
is needed on the dependence of the scaling law on the nanomorphology.

3.3.4 Effect of water and moisture concentration

Samples either fully water saturated or under 97% relative humidity were cut into 2.54 mm thick disks and were tested on the SHPB. Figure 24 compares the stress–strain relations at a strain rate of $\sim 300 \, s^{-1}$ for the dry, water-soaked and moisturized X-VOx samples cured either in acetone or in N3200. It is noted that these stress–strain curves are not complete due to the 1.5 ms total loading duration time limited by the length of the SHPB for testing at the moderate strain rate of $\sim 300 \, s^{-1}$. The shapes of stress–strain curves for three kinds of samples are similar. The stress–strain curves for the water-soaked samples are very close to those of dry samples, indicating that water does not have a very significant effect on the mechanical behavior in compression at high strain rates. By the same token, it may be noted that water absorption has a definite effect on the mechanical behavior at low strain rates, e.g., $5 \times 10^{-3} \, s^{-1}$ (see Fig. 11). At low strain rate, water trapped in the mesopores could escape gradually from the sample so that water-soaked X-VOx samples would be weaker than dry ones, indicating partial collapse of the structure. For X-VOx samples with lower initial density (0.417 g/cm^3), samples treated under 97% relative humidity have stress–strain relationships different from those of both water-soaked and dry samples, most probably due to associated volume shrinkage and the 90% increase in density. For X-VOx with higher initial density (0.592 g/cm^3), the water absorption weakens only slightly the mechanical properties at high strain rate, while samples under 97% relative humidity do not have much effect on their mechanical behavior.
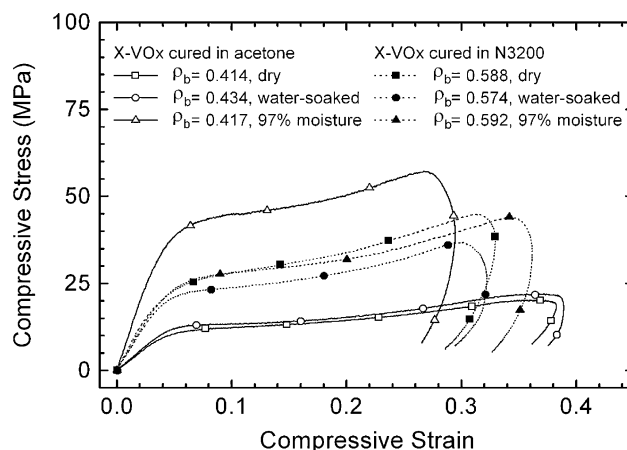

Fig. 23 Young's Modulus and yield strength as a function of mass bulk density (strain rate $\sim 300 \, s^{-1}$)

Fig. 24 Stress–strain curves for both water-soaked and moisturized X-VOx cured in acetone and in N3200
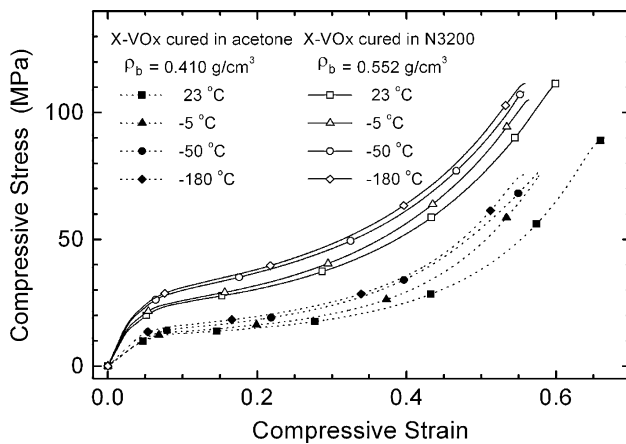
Fig. 25 Stress–strain curves of X-VOx at room and low temperatures (strain rate $\sim 1,300$ s^{-1})

3.3.5 The effect of low temperature

X-VOx disks (2.54 mm thick, 12.70 mm diameter) were tested on the SHPB at four temperatures, namely -180, -55, -5 °C, and room temperature), for two densities of X-VOx, (0.410 and 0.552 g/cm^3). The compressive stress–strain relations at strain rate $\sim 1,300$ s^{-1} are plotted in Fig. 25. Samples failed in testing so that these curves are complete stress–strain curves. The Young's modulus and 0.2% offset yield strength at each temperature are listed in Table 6. With the decrease in temperature, mechanical properties such as the yield strength increases by as much as 40% from room temperature to -180 °C. The mechanical properties of X-VOx increase with the decrease in temperature. For example, the Young's modulus (or yield strength) at -180 °C increases by 44% (22%) from the corresponding data at room temperature for X-VOx samples with density 0.552 g/cm^3. Furthermore, for the temperatures investigated, the stress-strain curves are shifted upward as the temperature decreases, indicating that the X-VOx has superior performance at lower temperatures. At cryogenic temperature, -180 °C, the X-VOx is still ductile, deforming to a compressive strain of more than 55%. The superior ductility of X-VOx at -180 °C is a feature not found with most materials such as BCC metals (e.g., steels) and polymers, which normally become brittle

at cryogenic temperatures [16]. For example, rubber behaves like a brittle glass when the temperature decreases to -180 °C, and can be crushed into powder with a slight impact. Similarly, polyurethane is rather brittle, failing at less than 5% compressive strain at cryogenic temperature. The entangled nanoworms in X-VOx allow the material to stay together under compression. This property makes X-VOx a material of choice for applications in energy absorption at low temperatures, or in liquid hydrogen (LH$_2$) storage tanks.

At high strain rates ($\sim 2,400$ s^{-1}), the yield strength (or ultimate compressive strength) is 8.91 (134 MPa) for X-VOx with densities 0.424. Digital image correlation was used to measure the surface strain through analysis of images acquired by ultra-high speed photography. Under compression, the compressive strain in the loading direction is nearly uniform, indicating that the failure of this nano-porous material (or open-cell nano-foam) is different from that of other foams such as polyurethane foams often used for thermal insulation, or as core for fiber-epoxy face sheets, which fails by propagation of instability (compaction) wave. The Poisson's ratio at high strain rates is 0.152. X-VOx samples failed at about $60-70$% compressive strain through axial splitting, but still remained as single pieces at both room and cryogenic temperatures at high strain rates. At room temperature the specific energy absorptions of X-VOx are 87.5 and 69.0 J/g at quasi-static compression and at strain rates $\sim 2,400$ s^{-1}, respectively. At a strain rate of $\sim 1,300$ s^{-1}, the specific energy absorption of X-VOx is 40.6 J/g at -180 °C, which is slightly lower than the value of 46.8 J/g obtained at room temperature. Observation of the morphology indicates that nanoworms in the X-VOx are fused to form thicker and longer nanoworms, thereby providing enhanced ductility in X-VOx not found with the native VOx.

4 Discussion

4.1 Young's modulus

Results for X-VOx listed in Table 3 are with samples having a length/diameter ratio of 2 and 1. As long as the

Table 6 Properties at strain rate ~ 300 s^{-1} of X-VOx under low temperatures

Bulk density (g/cm^3)	X-VOx cured in acetone				X-VOx cured in N3200			
	0.410				0.552			
Strain rate (s^{-1})	391	376	349	344	387	360	267	254
Temperature (°C)	23	-5	-50	-180	23	-5	-50	-180
E (MPa)	241 ± 17	244 ± 12	247 ± 4	250 ± 15	423 ± 26	447 ± 28	462 ± 28	609 ± 35
$\sigma_{0.2}$ (MPa)	7.3 ± 2.5	7.5 ± 0.5	8.2 ± 0.4	8.7 ± 0.6	14.8 ± 0.5	15.6 ± 1.4	16.9 ± 1.3	18.0 ± 0.6

samples are prepared with smooth and perfectly parallel end surfaces, the results are very consistent since the deformation in the specimen is uniform and the uniaxial compression obeys a one-dimensional (1D) stress condition. However, if samples are not prepared properly, results can differ, especially for native aerogels as they tend to break locally at small strains. On the other hand, for soft material with Young's modulus less than 0.5 MPa [35], if the length/diameter ratio is lower than 1 deformation in the specimen might not be uniform, which invalidates the 1D stress conditions in the uniaxial compression and leads to error in the property determination.

Property data are also compared with our previous results with X-SiO$_2$ aerogels [5]. In bending tests, if the elementary beam theory is used to determine the flexural modulus, the ratio of the length to width/height should be 16 according to ASTM D790. However, preparation of slender X-VOx aerogels was not straightforward: samples could deform to a curved shape, or even fracture during preparation. In this work, in order to determine the modulus, we used a length/thickness ratio of 5.58 and considered thick beam analysis with the contribution of shear induced deformation included in the total deformation that leads to Eq. 1.

It is noted that for materials that contain polymers, such as the polymer nanoencapsulated vanadia as reported in this paper, the Young's modulus measured from quasi-static compression cannot be compared with the modulus determined from measurement of wave speeds, because the Young's modulus determined from measurement of wave speed is the kind of modulus associated with high frequencies, at which the Young's modulus is usually higher. For example for PMMA, the Young's modulus measured from wave speeds at 5 MHz is 6.1 GPa, while the Young's modulus at a strain rate of 10^{-3}/min is only 3.1 GPa [36]. By the same token, while for native aerogels (i.e., those that contain no polymer), comparison of the modulus from compression (or bending) with that measured from wave speed determination can provide validation of the measurement, the same comparison for polymer crosslinked vanadia aerogels cannot provide assurance on the validity of the measurement of Young's modulus from quasi-static compression or bending tests.

4.2 Moisture absorption

It is noted that Fig. 5a and b show two distinct behavior patterns that appear to be intrinsic to the crosslinked vanadia aerogels. When X-VOx with density 0.417 g/cm^3 was exposed to 97% relative humidity, the mass was not affected much by moisture, possibly because the conformal polyurea coating, which was relatively thin, did not absorb much moisture. However, the volume of the monolith was

decreased significantly, possibly because of the rearrangement of the nano-worms due to hydrolysis and re-connection of the polymer strands at the contact points of the nano-worms under high relative humidity. On the contrary, in X-VOx with density 0.592 g/cm^3, there was a thicker polyurea coating on the vanadia nanoparticles so that the polymer would provide for a much stiffer entangled structure, similar to what is shown in Fig. 14a with a higher dimensional stability.

For X-VOx with density 0.414 g/cm^3, the Young's modulus of 242 MPa given in Table 2 is for dry samples at strain rate 370 s^{-1}. After the X-VOx sample has been subject to 97% relative humidity for 1,500 h, the sample density has increased to 0.816 g/cm^3 (due primarily to the shrinkage in volume), giving a density ratio of 1.97. Since the Young's modulus follows a power law relationship with density, with an exponent of 1.83 as listed in Table 5, the Young's modulus for the water-saturated sample is estimated to increase to 837 MPa; but since under high strain rate, water could carry load as well, the actual Young's modulus is 1,227 MPa. These results appear to indicate that the bulk density based scaling law does not apply for water-saturated samples.

At low strain rates, water trapped in the mesopores of vanadia not only weakens the links between nanoworms, but it also has sufficient time to flow out of the pores under the applied load so that its viscosity does not contribute much to the strength of the material, which overall shows a weaker behavior. However, at high strain rates, owing to its viscosity, water cannot escape from the mesopores during the very short time the load is applied. Hence, in comparison with the weakening effect of water at the interparticle links, the load-carrying capability of water itself gives a dominant contribution to the strength of the material, so that water-saturated X-VOx samples show stiffened behavior at high strain rates in comparison with dry X-VOx. This result is consistent with analogous observations in alcogels [31], in which the pore-filling solvent actually carries partially the applied load allowing the overall mechanical behavior to be better than that of the dry samples.

4.3 Energy absorption diagrams

As a type of mechanically strong aerogel, X-VOx may find uses for energy absorption applications in vehicle crash protection, armor, or landing gear of space modules on cryogenic environments. The specific energy absorption of 87.5 J/g for X-VOx at low strain rate is higher than that of polymethacrylimide (PMI) or Rohacell foam, that can achieve specific energy absorption up to around 35.0 J/g [25, 37], which is often considered a high value in engineering applications [25]. For full characterization of the

energy absorption capability of X-VOx at different peak stress levels, we have constructed energy absorption diagrams (Fig. 26). The normalized energy absorption, defined as the energy density W (area enclosed by the stress-strain curve up to a peak stress σ_p) divided by a reference modulus E_s, namely, W/E_s, is plotted against a function of the normalized peak stress σ_p/E_s, at a given density, strain rates and temperature [25]. For our purposes, E_s is taken as 1 GPa. Figure 26a–c show the energy diagrams of X-VOx, with the density, strain rate and temperature effects, respectively. The energy absorption curves of X-VOx show the envelope lines, tangential to the shoulders of individual curves. The shoulder corresponds to the densification stress σ_D and the densification strain ε_D, and can be obtained from the stress–strain curves. The slopes of the energy absorption with logarithm scale were determined to be 0.251, 0.204 and 0.237 for X-VOx from Fig. 26a–c, respectively. These diagrams can be used for future selection of X-VOx for energy absorption applications. The energy absorption of PMI polymer foam [37] with 3.73 GPa Young's modulus and 1.2 g/cm^3 skeletal density is enclosed and compared with X-VOx as shown in Fig. 26a. The normalized energy absorption and stress of PMI foam were one order of magnitude less than that of X-VOx, indicating that X-VOx possesses superior energy absorption capabilities.

5 Conclusion

Crosslinked vanadia aerogels have been developed by conformal nano-encapsulation of the fibrous skeletal framework of native vanadia aerogels with a 4 nm thick layer of diisocyanate-derived polymer. From XRD, the native vanadia is composed of $V_3O_7 \cdot H_2O$, which vanadium (IV) was reduced during processing from vanadium (V). The crosslinked vanadia with bulk density of 0.421 g/cm^3 consists of 82% polymer, 3% water and a balance of vanadia (15%). X-VOx has potential for engineering applications as it has overcome the brittleness and hydrophilicity of native VOx. Through DMA, a primary glass transition temperature was identified at 118.4 °C. In quasi-static compression, the X-VOx material was slightly weakened after it absorbed water, but the mechanical behavior is not sensitive to strain rates in the low strain rate range (4×10^{-4} to 4×10^{-2} s^{-1}). X-VOx has better mechanical properties at low temperatures, suitable for cryogenic structural application. The compressive behavior of X-VOx samples at high strain rates 50–2,500 s^{-1} was characterized using a long split Hopkinson pressure bar (SHPB). The dependence of Young's modulus and 0.2% offset yield strength on the mass density was determined and fitted into an equation. The surface full-field
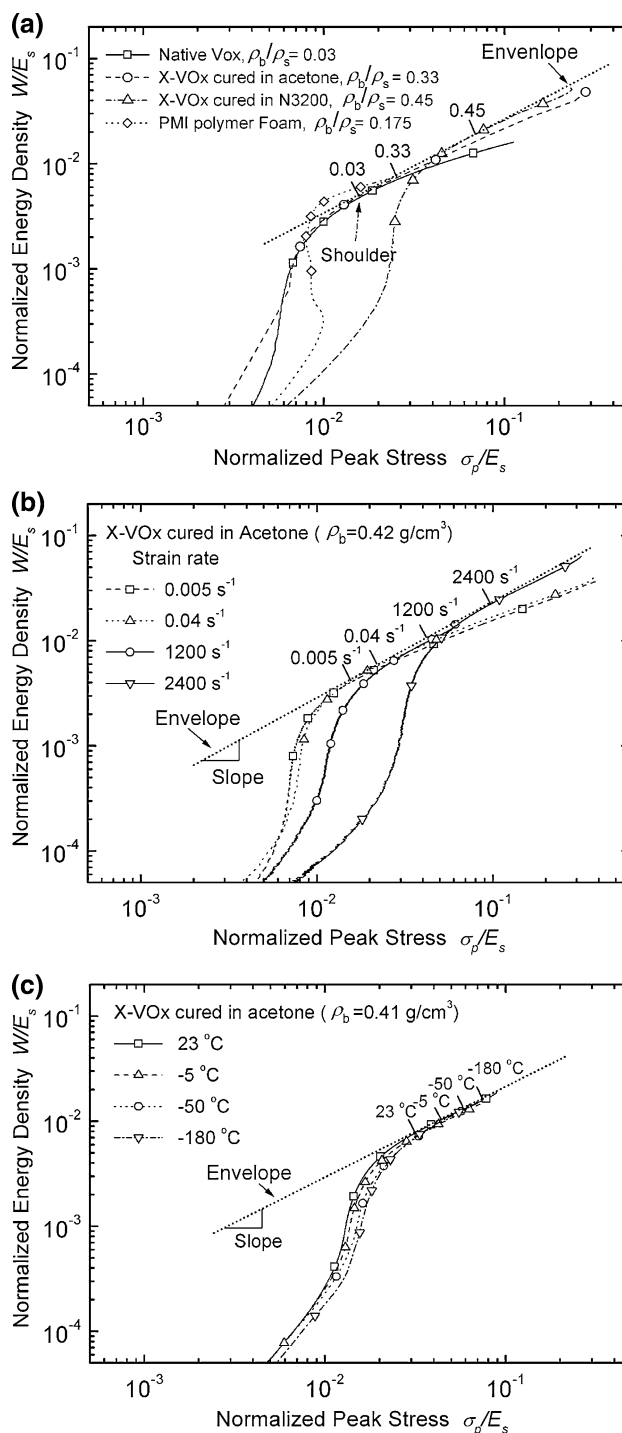

Fig. 26 Energy absorption diagrams for X-VOx. (a) effect of the bulk density at low strain rates as well as PMI foam, $E_s = 1$ GPa is used in all curves; (b) effect of strain rate at room temperature (bulk density, $\rho_b = 0.42$ g/cm^3; $\rho_b/\rho_s = 0.33$, where ρ_s is the skeletal density of X-VOx); (c) effect of temperature at strain rate 1300 s^{-1} (bulk density $\rho_b = 0.41$ g/cm^3; $\rho_b/\rho_s = 0.32$)

deformation of X-VOx samples was determined with digital image correlation on a series of high-speed deformed images on the SHPB. The axial deformation was relatively

uniform and no localized compaction occurred in compression at high strain rates; the Poisson's ratio was determined at 0.152. X-VOx samples failed at about 60–70% (80%) strain by axial splitting near the lateral surface at high (low) strain rates, respectively. The X-VOx has specific Young's modulus 544 (610 N m g^{-1}), specific yield strength at 12.0 (21.0 N m g^{-1}), specific ultimate strength 948 (316 N m g^{-1}), and specific energy absorption 87.5 (69.0 J g^{-1}) under quasi-static compression (and high strain rate), respectively. The good ductile properties can be traced back to the microstructural fusion of X-VOx nanoworm under both quasi-static loading and high strain rate loading. Under high strain rates, water absorption affects the mechanical properties of X-VOx less than at low strain rates, and moisture absorption has a more significant effect on the compressive behavior of X-VOx samples with lower densities than with higher ones. At −180 °C under impact, X-VOx exhibits a ductile behavior, bending the trend in most existing materials including several metals and polymers, which become brittle at low temperatures. X-VOx appears as an ideal multifunctional material for thermal insulation and impact protection in applications such as liquid hydrogen storage tanks, or vehicle and hard personal armor. An energy absorption diagram was constructed from stress–strain curves at various densities, strain rates and temperatures. The energy absorption capability of X-VOx surpasses that of PMI polymer foam. The slope of the energy absorption diagram was found in the range of 0.20–0.25. The energy absorption diagram can be used for material selection in energy absorption applications.

References

1. Pierre AC, Pajonk GM (2002) Chem Rev 102:4243
2. Leventis N, Sotiriou-Leventis C, Zhang G, Rawashdeh A-MM (2002) Nano Lett 2:957
3. Zhang G, Dass A, Rawashdeh A-MM, Thomas J, Counsil JA, Sotiriou-Leventis C, Fabrizio EF, Ilhan F, Vassilaras P, Scheiman DA, McCorkle L, Palczer A, Johnston JC, Meador MAB, Leventis N (2004) J Non-Cryst Solids 350:152
4. Bertino MF, Hund JF, Zhang G, Sotiriou-Leventis C, Tokuhiro AT, Leventis N (2004) J Sol-Gel Sci Technol 30:43
5. Katti A, Shimpi N, Roy S, Lu H, Fabrizio EF, Dass A, Capadona LA, Leventis N (2006) Chem Mater 18:285
6. Meador MAB, Fabrizio EF, Ilhan F, Dass A, Zhang G, Vassilaras P, Johnston JC, Leventis N (2005) Chem Mater 17:1085
7. Ilhan UF, Fabrizio EF, McCorkle L, Scheiman D, Dass A, Palzer A, Meador MAB, Leventis N (2006) J Mater Chem 16:3046
8. Capadona LA, Meador MAB, Alunni A, Fabrizio EF, Vassilaras P, Leventis N (2006) Polymer 47:5754
9. Leventis N (2007) Acc Chem Res 40:874
10. Meador MAB, Vivod SL, McCorkle L et al (2008) J Mater Chem 18:1843
11. Leventis N, Mulik S, Wang X, Dass A, Patil VU, Sotiriou-Leventis C, Lu H, Churu G, Capecelatro A (2008) J Non-Cryst Solids 354:632
12. Leventis N, Vassilaras P, Fabrizio EF, Dass A (2007) J Mater Chem 17:1502
13. Livage J (1991) Chem Mater 3:578
14. Sudoh K, Hirashima H (1992) J Non-Cryst Solids 147:386
15. Sudant G, Baudrin E, Dunn B et al (2004) J Electrochem Soc 151:A666
16. Leventis N, Sotiriou-Leventis C, Mulik S, Dass A, Schnobrich J, Hobbs A, Fabrizio EF, Luo H, Churu G, Zhang Y, Lu H (2008) J Mater Chem 18:2457
17. Chaput F, Dunn B, Fuqua P et al (1995) J Non-Cryst Solids 188:11
18. Chen W, Zhang B, Forrestal MJ (1999) Exp Mech 39:81
19. Frew DJ, Forrestal MJ, Chen W (2002) Exp Mech 42:93
20. Chen W, Lu F, Cheng M (2002) Polym Test 21:113
21. Luo H, Lu H, Leventis N (2006) Mech Time-Depend Mater 10:83
22. Knauss WG, Zhu W (2002) Mech Time-Depend Mater 6:231
23. Lu H, Cary PD (2000) Exp Mech 40:393
24. Dutoit DCM, Schneider M, Fabrizioli P, Baiker A (1997) J Mater Chem 7:271
25. Gibson LJ, Ashby MF (1997) Celluar solids: structure and properties-2nd ed, Cambridge University Press
26. Gray GT (2000) Classic split-Hopkinson pressure bar technique. In: Mech Test Eval, ASM Handbook, vol 8, 462 pp
27. Chen W, Zhou B (1998) Mech Time-Depend Mater 2:103
28. Fricke J (1990) J Non-Cryst Solids 121:188
29. Grob J, Schlief T, Fricke J (1993) Mater Sci Eng A168:235
30. Gross J, Fricke J (1995) NanoStruct Mater 6:905
31. Woignier T, Phalippou J, Hdach H et al (1992) J Non-Cryst Solids 147:672
32. Scherer GW, Smith DM, Qiu X et al (1995) J Non-Cryst Solids 186:316
33. Scherer GW (1998) Advan Colloid Interface Sci 76:321
34. Woignier T, Reynes J, Alaoui AH et al (1998) J Non-Cryst Solids 241:45
35. Miller K (2005) J Biomech 38:153
36. Lu H, Zhang XH, Knauss WG (1997) Polym Eng Sci 37:1053
37. Daphalapurkar NP, Hanan JC, Phelps NB, Bale H, Lu H (2008) Mech Adv Mater Struct, in press